

NUMERICAL AND EXPERIMENTAL INVESTIGATION OF ULTRASONIC
EMBOSSING TECHNIQUE FOR FABRICATION OF THERMOPLASTIC
MICROFLUIDIC DEVICES

A THESIS SUBMITTED TO
THE GRADUATE SCHOOL OF NATURAL AND APPLIED SCIENCES
OF
MIDDLE EAST TECHNICAL UNIVERSITY

BY

FERAH ÇOĞUN

IN PARTIAL FULFILLMENT OF THE REQUIREMENTS
FOR
THE DEGREE OF DOCTOR OF PHILOSOPHY
IN
MECHANICAL ENGINEERING

MAY 2018

Approval of the thesis:

**NUMERICAL AND EXPERIMENTAL INVESTIGATION OF ULTRASONIC
EMBOSSING TECHNIQUE FOR FABRICATION OF THERMOPLASTIC
MICROFLUIDIC DEVICES**

submitted by **FERAH ÇOĞUN** in partial fulfillment of the requirements for the degree of **Doctor of Philosophy in Mechanical Engineering Department, Middle East Technical University** by,

Prof. Dr. Halil Kalıpçılar
Dean, Graduate School of **Natural and Applied Sciences** _____

Prof. Dr. M. A. Sahir Arıkan
Head of Department, **Mechanical Engineering** _____

Prof. Dr. M. A. Sahir Arıkan
Supervisor, **Mechanical Engineering Dept., METU** _____

Asst. Prof. Dr. Ender Yıldırım
Co-Supervisor, **Mechanical Eng. Dept., Çankaya University** _____

Examining Committee Members:

Asst. Prof. Dr. Ulaş Yaman
Mechanical Engineering Dept., METU _____

Prof. Dr. M. A. Sahir Arıkan
Mechanical Engineering Dept., METU _____

Asst. Prof. Dr. Kıvanç Azgın
Mechanical Engineering Dept., METU _____

Assoc. Prof. Dr. Barbaros Çetin
Mechanical Engineering Dept., Bilkent University _____

Asst. Prof. Dr. Çağlar Elbüken
National Nanotechnology Research Center, Bilkent University _____

Date: 30 May 2018

I hereby declare that all information in this document has been obtained and presented in accordance with academic rules and ethical conduct. I also declare that, as required by these rules and conduct, I have fully cited and referenced all material and results that are not original to this work.

Name, Last name : Ferah Coğun

Signature :

ABSTRACT

NUMERICAL AND EXPERIMENTAL INVESTIGATION OF ULTRASONIC EMBOSSING TECHNIQUE FOR FABRICATION OF THERMOPLASTIC MICROFLUIDIC DEVICES

Çoğun, Ferah

Ph.D., Department of Mechanical Engineering

Supervisor: Prof. Dr. M.A. Sahir Arıkan

Co-Supervisor: Asst. Prof. Dr. Ender Yıldırım

May 2018, 87 pages

In this study, numerical models and experimental results were presented to describe mechanisms of hot embossing (HE) and ultrasonic embossing (UE) for fabrication of thermoplastic microfluidic chips. The substrates were embossed using micromilled aluminum molds in both techniques. Effects of embossing temperature, time, and force on performance outputs (replication rates and channel symmetry) were investigated numerically and experimentally in HE. Experimental results revealed the importance of temperature on performance outputs, whereas time and force have less effect. The experimental and finite element (FE) analyses emphasized the strong dependency of the channel skewness on substrate flow characteristics. In this study UE is considered as an alternative to HE since microfluidic channel embossing time is few seconds. The substrate deformation and temperature distribution across the mold and the substrate in UE were investigated using an FE model. The findings were verified with experiments using 3 mm thick PMMA substrate and a mold with straight channels. The mold pattern was replicated in 5 s at room temperature with high replication rates (99.5% in width and 100% in depth). A process-affected zone in the shape of a semi-circle observed in the experiments was proven by FE and thermal camera analyses to be bounded by the isothermal surface at the glass transition temperature of the substrate (107°C). Sealing of the fabricated channels were achieved by solvent-assisted thermo-compressive bonding in HE and UE. A

hydrogel droplet generator chip was designed and fabricated to demonstrate the suitability of the UE and micromilled mold for microfluidic device fabrication.

Keywords: Ultrasonic embossing, hot embossing, microfluidic, thermoplastic, modelling.

ÖZ

TERMOPLASTİK MİKROAKIŞKAN CİHAZLARIN ÜRETİMİ İÇİN ULTRASONİK BASKI TEKNİĞİNİN NUMERİK VE DENEYSEL OLARAK İNCELENMESİ

Çoğun, Ferah
Doktora, Makina Mühendisliği Bölümü
Tez Yöneticisi: Prof. Dr. M.A. Sahir Arıkan
Ortak Tez Yöneticisi: Dr. Öğr. Üyesi Ender Yıldırım

Mayıs 2018, 87 sayfa

Bu çalışmada termoplastik mikroakışkan cihazların üretimine dönük olarak sıcak baskı (SB) ve ultrasonic baskı (UB) tekniklerinin mekanizmalarını tanımlamak için numerik modeller ve deneysel sonuçlar sunulmuştur. PMMA malzemeler her iki teknikte mikrofrezelenmiş alüminyum kalıplar kullanılarak basılmıştır. SB tekniğinde baskı sıcaklığının, süresinin ve kuvvetinin performans çıktılarına (replikasyon oranı ve kanal simetrisi) etkileri numerik ve deneysel olarak incelenmiştir. Deneysel sonuçlar sıcaklığın performans çıktıları üzerinde önemli etkisini, sürenin ve kuvvetin düşük etkisini ortaya çıkarmıştır. Deneysel ve sonlu eleman (SE) analizleri malzemenin akış karakteristiklerinin kanal kayıklığındaki güçlü etkisini vurgulamıştır. Bu çalışmada UB tekniği mikrokanal üretim süresi birkaç saniye olduğundan SB'ye alternatif olarak değerlendirilmiştir. Geliştirilen SE modeli kullanılarak, UB tekniğinde malzeme deformasyonu ve kalıp ve malzeme kesitinde sıcaklık dağılımı incelenmiştir. Bulgular, 3 mm kalınlığında PMMA malzeme ve düz kanal desenli kalıp kullanılarak yapılan deneylerle teyid edilmiştir. Kalıp desenleri oda sıcaklığında 5 saniyede yüksek replikasyon oranlarında (genişlikte 99.5%, derinlikte 100%) basılmıştır. SE ve ısı kamera analizleri, UB deneylerinde yarı daire geometrisinde işlemde etkilenmiş bir bölgenin (İEB) malzemenin cam geçiş sıcaklığındaki (107°C) izo-sıcaklık yüzeyi ile çevrelendiğini ispatlamıştır. SB ve UB yöntemleri ile üretilmiş kanalların kapatılması solvent-

destekli sıcak-baskı yöntemi ile başarıyla sağlanmıştır. Mikroakışkan cihaz üretiminde UB işleminin ve kalıpların mikrofrezle ile üretiminin uygunluğunu göstermek için bir hidrojel damla üretici çip tasarlanmış ve üretilmiştir.

Anahtar Kelimeler: Ultrasonik baskı, sıcak baskı, mikroakışkan, termoplastik, modelleme.

To My Parents

ACKNOWLEDGMENTS

The author wishes to express her deepest gratitude to her supervisor Prof. Dr. M.A. Sahir Arıkan and co-supervisor Dr. Ender Yıldırım for their guidance, advice, criticism, encouragements and insight throughout the research.

The technical assistance of Mr. Levent Yeltekin is gratefully acknowledged.

Finally, yet importantly, I am indebted to my beloved family members for their understanding, support, endless patience and encouragement through the study.

TABLE OF CONTENTS

ABSTRACT	v
ÖZ	vii
ACKNOWLEDGMENTS	x
TABLE OF CONTENTS	xi
LIST OF TABLES	xiii
LIST OF FIGURES	xiv
CHAPTERS	
1. INTRODUCTION	1
1.1 Plastic Microfabrication Techniques	1
1.1.1 PDMS Molding	1
1.1.2 Micromilling, Injection Molding and Hot Embossing (HE)	2
1.1.3 Ultrasonic Embossing (UE)	3
1.2 Review of Ultrasonic Embossing (UE)	4
1.3 Objective of Thesis	15
1.4 Organization of the Thesis	16
2. HOT EMBOSSING	19
2.1 Working Principle	20
2.2 Numerical Analysis	21
2.3 Experimental Work	23
2.4 Demonstration of Hot Embossing	30
2.5 Discussion and Conclusion	32
3. ULTRASONIC EMBOSSING	35
3.1 Working Principle	35
3.2 Numerical Analysis	36

3.3 Experimental Work.....	40
3.3.1 Process Affected Zone (PAZ)	42
3.3.2 Load Measurement	45
3.3.3 Temperature Measurement of PAZ.....	47
3.3.4 Comparison of Experimental Work with FEM Results for PAZ	51
3.4 Discussion and Conclusion.....	52
4. FABRICATION OF A DROPLET GENERATOR CHIP BY UE.....	55
4.1 Droplet Generator	56
4.1.1 Modeling of Droplet Generator	57
4.1.2 Fabrication of the Chip	62
4.1.3 Chip Characterization	64
4.2 Discussion and Conclusion.....	67
5. CONCLUDING REMARKS AND FUTURE WORK.....	69
REFERENCES	73
CURRICULUM VITAE	85

LIST OF TABLES

TABLES

Table 1.1 Comparison of common polymer-based fabrication techniques with UE.	3
Table 2.1 Dimensions of mold straight protrusions [66].....	25
Table 2.2 HE parameters used in the experiments [66].....	26
Table 3.1 PMMA material properties [80].	38
Table 3.2 Material properties of the mold (aluminum 7075).	38
Table 4.1 Dimensions of the channels.....	61

LIST OF FIGURES

FIGURES

Figure 1.1 (a) Aluminum molding tool cross-section. (b) The polymer view after UE [28].	5
Figure 1.2 (a) Aluminum welding tool cross-section. (b) The polymer channel view after welding [28].	5
Figure 1.3 Embossed pattern of PC. (a) Without ultrasonic vibration. (b) With ultrasonic vibration [30].	7
Figure 1.4 Embossed pattern of mold on (a) PS, (b) PP, (c) PETG materials [31]....	8
Figure 1.5 Ultrasonically hot embossed patterns using three PC foils (each 250 μm thick). (a) Without PE- Al_2O_3 powder. (b) With PE- Al_2O_3 powder between the foils [34].	10
Figure 1.6 (a) Embossed patterns of round shapes for micromixer. (b) SEM view of the embossed pattern of ridges [36].	12
Figure 1.7 Cross-section of the embossed channel with double layer (250 μm and 150 μm thick) films [36].	12
Figure 1.8 Cross-section of the aluminum film embossed on PP [36].	13
Figure 1.9 Replicated PDMS and PE nanoprotusions [37].	13
Figure 1.10 Replicated PDMS and PE nano-microstructures [37].	13
Figure 1.11 SEM of the pillar-type micromold replicated on PMMA [38].	14
Figure 1.12 SEM of the pore-type micromold replicated on PMMA [38].	14
Figure 2.1 Stages of HE, (a) substrate placement, (b) compression, (c) cooling and demolding, (d) embossed substrate [66].	20
Figure 2.2 (a) Mold and substrate; (b) right half of the substrate; (c) comparison of R1, R2, and R3 profiles [66].	21
Figure 2.3 Single replication cases: (a) on the left (LR), (b) at the center (CR), (c) on the right (RR). (d) Comparison of LR, CR, and RR profiles [66].	22

Figure 2.4 Comparison of RR and R3 profiles [66].	23
Figure 2.5 (a) HE press and heating plates, (b) embossed chip, (c) fabricated mold and its' protrusions [66].	24
Figure 2.6 (a)–(e) SEM images of the replicated channels embossed at 115°C, 8 kN, and 6 min settings by using 56, 105, 216, 310, and 436 μm protrusions. (f)–(j) microscope views of channels. (k)–(o) Channel profile plots for different temperatures (for 8 kN, 6 min) and the same mold width. (p) Illustration of the PMMA substrate [66].	28
Figure 2.7 (a) r_w and (b) r_d for different temperatures and mold feature widths (embossing force and time are 8 kN and 6 min, respectively). (c) r_w values at 115°C for different force and time settings [66].	29
Figure 2.8 (a) Shore-D hardness test [66], (b) DSC analysis of PMMA substrate.	29
Figure 2.9 S/N ratios for different process parameters for 105 μm mold feature width [66].	31
Figure 2.10 (a)–(d) Fabrication of the microfluidic chips.	31
Figure 2.11 A bonded microfluidic chip after dispensing dyed water for leakage test [66].	32
Figure 3.1 The stages of UE process.	36
Figure 3.2 Schematic view of (a) mold and PMMA, (b) meshing. (c) True stress-plastic strain of PMMA (at 1 s^{-1} strain rate) with varying temperature [81].	38
Figure 3.3 (a) Temperature, (b) equivalent plastic strain, and (c) von Mises stress distributions (for 5 s of UE at 25°C).	40
Figure 3.4 Details of the custom-made ultrasonic embossing test set-up.	41
Figure 3.5 (a) Section view of the embossed channel (b) the minor cracks at the bottom edges of the channel.	43
Figure 3.6 Average CD with (a) varying t_e settings at $T_e=100^\circ\text{C}$, (b) varying T_e settings at 5 s, (c) varying t_e settings at $T_e=25^\circ\text{C}$.	44
Figure 3.7 Representative view of PAZ.	45
Figure 3.8 r_w and r_d for different embossing temperatures ($t_e=5$ s).	45

Figure 3.9 (a) Load cell mounted to strain indicator and recorder, (b) bottom view of load cell, c) support plate, PMMA and mold arrangement, (d) mold, (e) support plate.	46
Figure 3.10 (a) Calibration line of the load cell, (b) variation of embossing force (F_{ad}) with embossing time for $t_e=5$ s, $T_e=25^\circ\text{C}$.	46
Figure 3.11 Schematic view of temperature measurement with thermal camera.	47
Figure 3.12 (a) Temperature distribution obtained from FEM. (b)-(f) Experimental temperature distribution across the mold and the substrate. (g) Section view of the experimentally embossed channel. (h) Isothermal lines overlaid with the section view of the channel.	49
Figure 3.13 T_{av} with varying t_e for (a) $T_e=25^\circ\text{C}$, (b) $T_e=100^\circ\text{C}$. The bars indicate the standard deviations of the measurements.	50
Figure 3.14 (a) FTIR analysis, (b) TGA and (c) DTA results.	50
Figure 3.15 Comparison of T_{av} for FEM and temperature results of thermal camera ($t_e=5$ s, $T_e=25^\circ\text{C}$).	51
Figure 4.1 Droplet generation in (a) T-junction geometry, (b) flow focusing geometry [105].	56
Figure 4.2 Schematic view of designed chip, (b) Modelling of the chip with electrical circuit analogy.	61
Figure 4.3 Flow rates of the inlet channels.	62
Figure 4.4 The droplet formations at various times.	62
Figure 4.5 (a) The mold pattern design, (b) micromilled mold pattern.	63
Figure 4.6 UE chip sealed with solvent assisted thermo-compressive bonding.	64
Figure 4.7 (a) DW droplets formed after junction, (b) stages of formation of DW droplets at the junction, (c) hydrogel droplets formed after junction, (d) arrangement of hydrogel droplets in the channel.	66
Figure 4.8 Distributions of (a) droplet size and (b) the average distance between the droplets (sample size=61).	67

CHAPTER 1

INTRODUCTION

1.1 Plastic Microfabrication Techniques

In the last two decades, the miniature devices for biomedical and biological applications (referred as lab-on-a-chip (LOC)) are realized by the improvement of microtechnology and micromachining methods. The LOC systems include microfluidic devices which could perform sample separation, detection, analysis and pretreatment functions strongly required for drug tests, health and cell monitoring and clinical solutions. These devices are sensitive, reliable, small, low cost, and capable of performing more than one test in parallel on the microchannels of the same substrate. These devices can be produced from variety of materials like silicon (Si) based materials, polymers, etc. The difficulties in the surface modification after the fabrication, unsuitability for biological applications (not biocompatible), long fabrication times and the need for the clean room environment for the Si based materials in microfluidic devices [1-3] lead to the introduction and development of polymer materials. Polymers are optically transparent, biocompatible, suitable for different surface modifications and highly reproducible. Also, fabrication processes are less expensive and much faster than Si based fabrication methods [4]. Different polymers (poly methyl methacrylate (PMMA), cyclic olefin copolymers (COC), polycarbonate (PC), polyimide (PI), polyethylene terephthalate (PET), polydimethylsiloxane (PDMS) are used for these purposes considering their favorable properties in different applications [1].

1.1.1 PDMS Molding

PDMS is the commonly used elastomer material in microfluidic devices [5]. PDMS molding is used for fabrication of PDMS devices [6-8]. In PDMS molding, a liquid PDMS poured into and cured in the mold. After curing, the PDMS is peeled off from the mold and a negative stamp of the mold, which includes the microfluidic channels, is created. However, PDMS is highly gas permeable elastomer material, has

uncontrollable wettability and hydrophobic characteristics [4, 7] which could be considered as a drawback in some microfluidic applications. So, the devices made by PDMS molding are unsuitable for commercial use [9-12].

1.1.2 Micromilling, Injection Molding and Hot Embossing (HE)

Thermoplastic devices are highly promising for the consideration of fabrication easiness, low cost, suitability for large volume production and no need for clean room facilities. Although, there are varieties of methods available for fabrication of thermoplastic microfluidic devices, the commonly used methods are micromilling, hot embossing and injection molding.

In micromilling method, milling tools are used for removing material from the thermoplastic substrate directly. The microchannels can be directly machined on to the final device in few minutes depending on the geometry with vertical sidewalls and good surface finish [13, 14]. However, the use of small diameter milling cutters (less than 100 μm) in machining small size and intricate channels makes the machining difficult due to undesired cutter deflections during cutting. Alternatively, micromilling method can be used for fabricating the mold which will be used for embossing and injection molding of the substrate [15, 16].

In injection molding, thermoplastic pellets are melted and injected into a heated mold cavity. When the injected material is solidified, it is released from the mold [17, 18]. Since the equipment and molds fabrication costs are high, it is mostly used in industrial applications with high production volumes [19].

In hot embossing (HE), the thermoplastic substrate is heated above its glass transition temperature and the heated mold with the protruding channels pattern is pressed to the substrate. After cooling, the embossed substrate is demolded from the mold. Since the process temperature and pressure in HE is lower than the injection molding, the cost of the equipment and mold fabrication are cheap. Since the cycle time of HE is higher than the injection molding [20], the injection molding is more suitable for mass production.

1.1.3 Ultrasonic Embossing (UE)

In order to reduce the cycle time and the equipment cost of the HE, an alternative method, ultrasonic embossing (UE) is introduced for fabrication of the thermoplastic microfluidic devices. The substrate is ultrasonically embossed in a few seconds to the mold. Thus, it is suitable for medium and high volume productions. Also, the equipment cost of the UE technique is low since it does not require heating of the substrate and mold as well as high embossing forces [21]. The thermal distortions are less compared to HE since the substrate is locally heated by the ultrasonic motion of the mold [22].

Table 1.1 compares the afore-mentioned thermoplastic microfluidic device fabrication techniques, namely micro milling, HE and injection molding, with UE in metrics of cost, cycle time and surface roughness. The surface roughnesses of the channels formed are depend on mold surface quality in HE, injection molding and UE processes whereas it depends on machining parameters in micromilling. Per chip (microfluidic device) cost is dramatically reduced in UE method especially for large production volumes due to low process time and equipment cost.

Table 1.1 Comparison of common polymer-based fabrication techniques with UE.

	Micromilling	HE	Injection Molding	UE
Surface Roughness	0.4-2 μm	Depends on mold quality	Depends on mold quality	Depends on mold quality
Cost per chip	137 \$ [23]	56-322 \$ [23]	2257 \$ [23]	~ 1 \$ *
Equipment cost	~ 30000 \$ [24]	~ 20000 \$ [24]	> 40000 \$ [24]	~ 750 \$ *
Cycle time per chip	5-30 min [24]	10-30 min [24]	10-30 s [24]	≤ 10 s *

* Authors' analysis based on fabrication of 200 microfluidic chips.

1.2 Review of Ultrasonic Embossing (UE)

In Cui et al. [25] study, a method for fabrication and assembling of electrical interconnecting surface mounted devices (SMDs) to form a flexible electronic board from polymer film (PVDF with 250 μm thickness) by UE was proposed. A mold (tool) pattern with 100 μm in height and width made of aluminum was manufactured with micromilling process. Effectiveness of the electrical interconnection was tested at elevated temperatures, humidity and bending load conditions. It was shown that the electrical interconnection is effective and stable and resistance changes of $<0.15\%$ were observed in bending of the SMD.

In Hung et al. [26] study, a new component for an ultrasonic vibration-assisted glass HE was enhanced and modified for high temperature use of ultrasonic vibrating system. During the forming process, forces were measured with a load cell placed inside the vacuum chamber. Flat and Fresnel structure HE were performed in the experimental phase of the study. In flat HE experiments, the force decreased quickly as ultrasonic vibration was applied indicating the softening of the glass. In Fresnel HE experiments, the step heights of the molded glass were improved with ultrasonic vibration.

In Khuntontong et al. [27] study, an antenna for radio frequency identification device (RFID) and a flexible membrane keyboard were fabricated with aluminum foil (10 μm thick) conductive paths on PP films (150 μm and 250 μm thick) by UE. The surface of aluminum material used as ultrasonic horn was micromilled as a protruding bar (500 μm height and 700 μm wide). In the middle of the top of the bar, two 100 μm deep and 500 μm wide grooves were opened to leave a cutting edge with 100 μm height and 100 μm width. 35 kHz ultrasonic vibration with 12 μm amplitude, 80 N force and 2 s duration was applied to the polymer. The results showed that the antenna circuits give the desired resonance frequencies and the keyboard can be implemented as an input device for a PC successfully.

In another study of Khuntontong et al. [28], a thermal micro flow sensor channel (100 μm high, 500 μm wide, and 1 cm long) from two PP films (each 250 μm thick) which was crossed by a 50 μm diameter gold wire was fabricated by UE. The aluminum

mold (figure 1.1) was micromilled to form 500 μm height, 500 μm width and 10 mm length pattern. Ultrasonic vibration with 9 μm amplitude at 100 N force was applied to the PP films. The 100 μm deep groove was embossed in 150 ms. Hold time of 500 ms was given for cooling of the polymer. An aluminum micromilled horn (figure 1.2) for ultrasonic welding (35 kHz) was used to seal the microchannel with 150 μm thick PP film. In welding process, 50 N force with 9 μm ultrasonic amplitude was applied for 200 ms (500 ms hold time for cooling). The wire of the sensor was heated by 15°C in water and the response time of the sensor was found as 24 ms. It was stated that more investigations were required for better understanding of the polymer flow for complete filling of the molds.

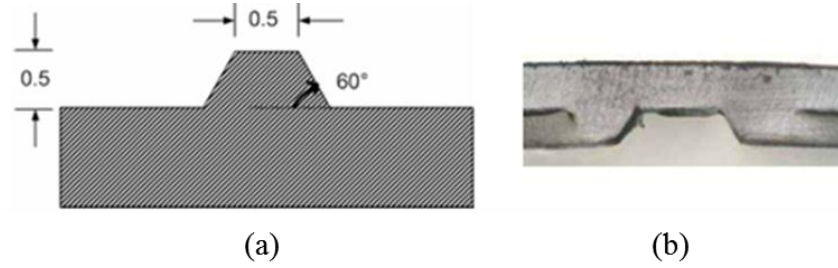


Figure 1.1 (a) Aluminum molding tool cross-section. (b) The polymer view after UE [28].

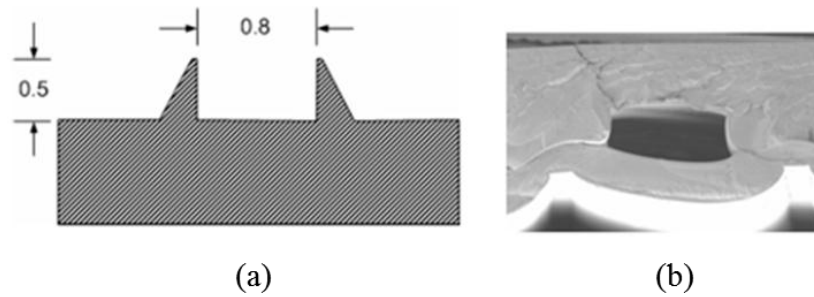


Figure 1.2 (a) Aluminum welding tool cross-section. (b) The polymer channel view after welding [28].

In Li et al. study [29], a method of fabricating molded interconnect devices (MID) conductor paths into a copper layer (18 μm thick) on polymer foils by UE was introduced. In Khuntontong et al. [27] study, conductor paths were formed by punching aluminum lines (from a 150 μm thick aluminum foil) on a plastic substrate surface. A difficult manual metal scraping removal process was required after the UE. This problem was solved by embossing interruptions into a continuous metal sheet. The UE was performed by using three types of PVC foils (each 150 μm thick) at 6 μm amplitude, 2.4 kN force, 250 ms ultrasonic time and 500 ms hold time. The conductor paths with 400, 300 and 250 μm widths were replicated at 2.5 kN force and 450 ms ultrasonic time. Two LEDs, five surface mount (SM) resistors, two capacitors and two transistors were ultrasonically welded onto the circuit board of multi-vibrator circuit at 6 μm vibration amplitude, 170 N force and 200 ms UE time settings. The authors emphasized the need for further investigation for development of multilayer circuits and circuit boards with larger dimensions.

Liao et al. [21] described different fabrication techniques of mold for UE process. In the study, micromilling, electroplating and micro electrochemical and micro electro discharge machining methods were defined for mold fabrication. It was stated that micromilling of aluminum is the most flexible and low-cost method for mold fabrication despite its limits in achieving small structures and in machining harder materials than aluminum. They recommended the use of combined lithography, especially X-ray lithography and electroplating methods for fabrication of smaller micro structures.

In Mekaru et al. study [30], ultrasonic nanoimprint lithography system software was modified so that ultrasonic vibration of 19 kHz frequency was applicable for molding process. Micro patterns with seven sizes of entrance (100 μm^2 to 1.2 mm^2 area) were used on the electroformed Ni mold. Ultrasonic vibration was generated on PC sheet at maximum amplitude of 1.8 μm . Reduced bubble defect with impressing ultrasonic vibration in the patterns was observed. It was also found that the ultrasonic vibration improved significantly the molding rate (ratio of the successful patterns to total patterns) for the case of micro HE (figure 1.3). The authors concluded that the

ultrasonic vibration was well suited for improving the process especially at low forces whereas high force was blocking the progression of ultrasonic vibration.

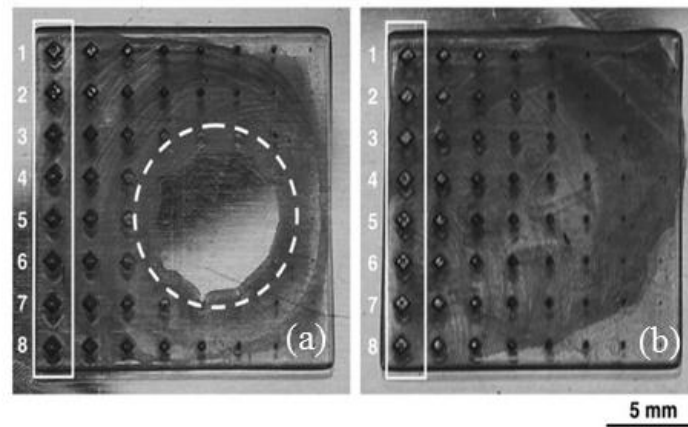


Figure 1.3 Embossed pattern of PC. (a) Without ultrasonic vibration. (b) With ultrasonic vibration [30].

Gielen et al. [31] proposed an alternative fabrication method for printed circuit board (PCB). In their study a single layer electrical PCB pattern with 200 μm depth was micromilled on brass material. PETG, PS and PP polymers were used in the tests (figure 1.4). They emphasized on incomplete filling in some edges due to the insufficient force. The material was melted around the most densely elevated mold area and material has to move through narrow flow paths in order to fill the less dense areas. It was reported that, PETG was the only material embossed successfully among the others. Since the PS has low heat diffusivity coefficient, the surface of PS was overheated before the molding process. Also, the PP was not suitable for hot forming processes due to its non-uniform material melting characteristics. The authors believed that other polymers which have higher heat diffusion coefficient would give better results. Moreover, for a localized material flow, pattern of the mold must be designed carefully so that the protruding area was distributed evenly over the surface.

In Sackmann et al. study [32], UE, ultrasonic welding, thermoforming, ultrasonic punching and ultrasonic riveting processes as well as applications like flow sensors, heat exchangers, micro mixers and electronic circuit boards were described in detail.

The effect of mold heating on ultrasonic welding performance was studied by using molds with 150 μm , 250 μm , and 300 μm width, 8 mm long and up to 800 μm depth grooves. Three PVC foils (each 250 μm thick) were used in the UE. Better filling of structures was observed since heating of the mold results in a delay of the solidification process. The authors reported an 80°C mold limiting temperature for PVC whereas higher temperatures caused deformations in demolding and undesired chemical colorings of the substrate. It was found that the UE time was a more effective parameter than the mold temperature on embossing large patterns (1 mm width, 0.7–1.2 mm depth). A gastight chamber was used to prevent the decomposition of polymers and to ease the filling of the grooves. Yet, the tests with argon, nitrogen and reduced pressure in a vacuum chamber did not make considerable improvement in replication rates compared to embossing results at ambient air. The authors concluded that several millimeters wide or a few micrometers high bars or grooves can't be embossed to most of the polymers due to the energy distribution over the large area causing insufficient melting.

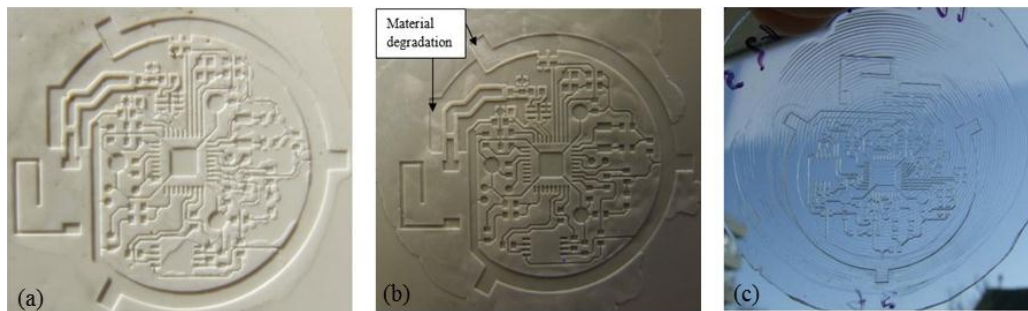


Figure 1.4 Embossed pattern of mold on (a) PS, (b) PP, (c) PETG materials [31].

Burlage et al. [22] showed a decrease in embossing force and time by up to a third using two polymer layers instead of one. A 35 kHz ultrasonic machine with 900 W power, 12 μm maximum amplitude and 745 N maximum force was used in the experimental phase of the study. Two mixers, one with a smooth channel and the other

with a channel with diagonal ridges, were fabricated and tested. In the tests, mixing was incomplete over the mixing length of 25 mm in smooth channels whereas it was complete for the mixers with the ridges. The authors also produced a mold to show suitability of UE process to fabricate the MID. A 10 mm long, 700 μm wide and 500 μm high bar was milled on the aluminum mold surface. A 100 μm deep and 500 μm wide chamfer was milled in the middle of the bar to form a sharp cutting edge. A 250 μm thick PP and a liquid thermoplastic resin which was spin-coated (50-80 μm thick) on an aluminum film (10 μm thick) were used. The authors also studied the effect of ultrasonic time and force on embossing depth for a 0.5 mm high and wide bar on PP film. It was found that the higher embossing depth was achieved in a shorter time at higher forces.

In Luo et al. [33] study, a double-side thermal assisted UE method was introduced. Ultrasonic welding machine (30 kHz) with 6–60 μm amplitude, 680 N maximum force and 30 s maximum ultrasonic time were used in the study. Silicon molds were fabricated using wet etching. 1 mm and 2 mm thick PMMA substrates were used in the experiments. Before the ultrasonic vibration was applied, the substrates were preheated to 40–60°C. The process parameters (ultrasonic amplitude, force, time and thermal assisted temperature) were varied according to orthogonal array experiments for replication of PMMA. Also, the effects of substrate thickness, pattern style and density on replication rate were investigated. It was found that, for the 1 mm thick substrate, the replication rate achieved was 97.1% - 99.9% whereas it was 2.7% - 55.6% for the 2 mm thick substrate. It was concluded that a thinner substrate reaches higher replication rate due to the higher surface and internal stresses exposed than a thicker one. It was shown that for the upper surface replication the ultrasonic amplitude and for lower surface replication the thermal assisted temperature was the key parameters. On the other hand, the ultrasonic force had the highest impact on replication homogeneity for both surfaces. The experiments indicated that it was difficult to replicate concave mold, and more energy was required to replicate heavy density microstructure.

Kosloh et al. [34] studied the heat generation and distribution during the UE process. Force distribution was measured by piezo-electric and pyro-electric PVDF foils

between polymer layers and heat distribution was obtained by using thermocouples in the molds. Aluminum molds were milled for UE. The effect of temperature distribution in a stack polymer layers was investigated by combining with an even (250 μm thick) and roughened foils (pre-structured foils with 500 μm thickness) from PC in several arrangements. Satisfactory embossing results were obtained at shorter times and with less force with the combination of even and pre-structured foils. It was also shown that the addition of PE- Al_2O_3 powder between the foil-layers improved the embossing performance resulted in higher absorbed ultrasonic energy which generated more melt (figure 1.5).

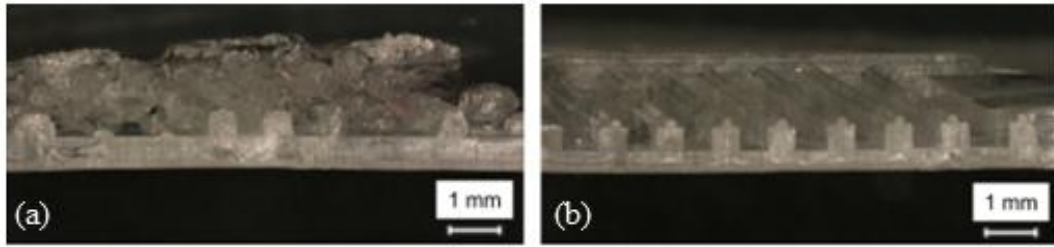


Figure 1.5 Ultrasonically hot embossed patterns using three PC foils (each 250 μm thick). (a) Without PE- Al_2O_3 powder. (b) With PE- Al_2O_3 powder between the foils [34].

In Mekaru et al. study [35], the effect of ultrasonic vibration on HE and thermal nanoimprint was investigated. In the study, a piezoelectric actuator was used for the generation of ultrasonic vibration in a vacuum HE system. An ultrasonic machine (15 kHz) with 900 W power and 16 ± 2 μm amplitude was used. The mold was formed by Ni electroforming of Si dry etched pattern. Mold had a five different pattern entrances range from 100 to 540 μm in length with 260 μm depth. PC was used as molding material. The best molding in the vacuum HE was obtained at 180°C mold temperature, 0.5 kN contact force and 60 s time. It was observed that the contact force and time reduced down to 1/3 and 1/12 of atmospheric HE values, respectively, by using ultrasonic vibrations. It was also reported that the progression of ultrasonic vibration was inhibited at high contact forces. The authors also measured the molding

accuracies of various patterns ranging $100\ \mu\text{m}^2$ - $1.2\ \text{mm}^2$ area produced by ultrasonic vibration (19 kHz) at maximum amplitude of $1.8\ \mu\text{m}$. The embossed patterns showed bubble defects due to residual gas when ultrasonic vibration was not in use. It was seen that the bubble defect was reduced or completely prevented when ultrasonic vibration was used. Also, the effect of thermal nanoimprint on replication rate with ultrasonic vibrations was tested experimentally on PC substrate. It was shown that replication of nano-patterns with 500 and 750 nm widths can be achieved at lower temperatures (about 160°C) than without thermal nanoimprint system.

In Khuntontong study [36], the UE was shown to be a suitable technique for the fabrication of polymer microstructures in a couple of seconds. In the experiments, ultrasonic machine (works at 20, 35 and 70 kHz frequencies) was used to UE $250\ \mu\text{m}$ thick PP films at various vibration amplitudes (up to $10\ \mu\text{m}$). Aluminum molds were fabricated with micromilling. It was shown that frequency, amplitude, time, pressure and polymer type were the important parameters for controlling UE process and the achievable aspect ratio, overall pattern size, and minimum and maximum structure height were the performance measures of UE. In the study, micro mixers, micro thermal flow sensors and MID (figure 1.8) were manufactured with UE. The mixing channel with a T- junction inlet and an outlet (figure 1.6(a)) was a 25 mm long, $100\ \mu\text{m}$ high, and $500\ \mu\text{m}$ wide one. The ridges molded onto the mixing channel (figure 1.6(b)) had $20\ \mu\text{m}$ high, $250\ \mu\text{m}$ wide and orientated at 45° with the channel walls. It was found that the ridges reduced the mixing time by a factor of 4. In the study, $100\ \mu\text{m}$ high, $500\ \mu\text{m}$ wide and 1 cm long micro thermal flow sensor (figure 1.7) with $150\ \mu\text{m}$ depth embedded by a $50\ \mu\text{m}$ diameter gold wire onto PP films was fabricated. The test results showed that reaction times of the sensor was 24 ms after switching on and 20 ms after switching off the piezo-actuated micro diaphragm pump at 0.5 Hz. The author reported that for $200\ \mu\text{m}$ thick polymers, a 35 kHz was a suitable frequency. The UE time should be limited to 160% of the saturating time to prevent cracking and burning of the polymers. In order to obtain deeper grooves, higher pressures as well as shorter UE time was required. It was highlighted that the amplitude of vibration was the most effective parameter to increase the heat input to the substrate.

Lee et al. [37] investigated the replication of PE and PDMS (500 μm thick) nano-micro hierarchical structures. Ni nano-molds and nano-micromolds were fabricated using Ni electroplating technique. The optimum ultrasonic time was found as 1.5 s and 3 s for nanoprotusions (figure 1.9) and nano-micro hierarchical structures (figure 1.10), respectively. The replication rate of $1 \times 1 \mu\text{m}$ nanoprotusions was 62% in width for both PDMS and PE substrates. An 87% and 67% replication rates in height were found for PE and PDMS substrates, respectively. The fabricated structures were coated with plasma polymerized fluorocarbon of a hydrophobic nature to modify superhydrophobic surfaces. By this way, the contact angle was increased from 106° to 125° (nanostructured surface) and finally to 160° (nano-microstructured surface) so that the surface became superhydrophobic.

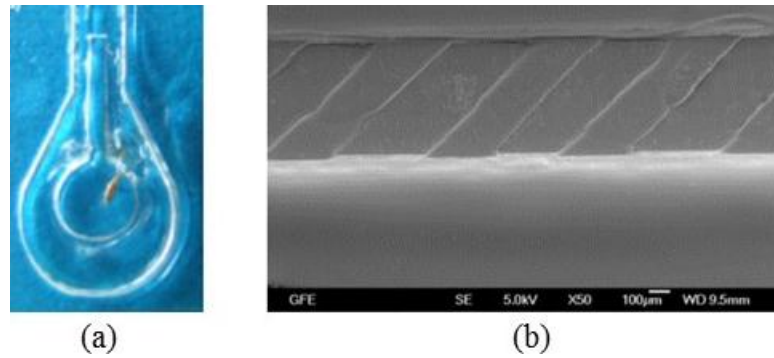


Figure 1.6 (a) Embossed patterns of round shapes for micromixer. (b) SEM view of the embossed pattern of ridges [36].



Figure 1.7 Cross-section of the embossed channel with double layer (250 μm and 150 μm thick) films [36].

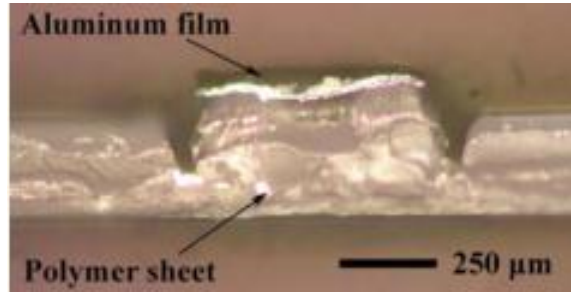


Figure 1.8 Cross-section of the aluminum film embossed on PP [36].

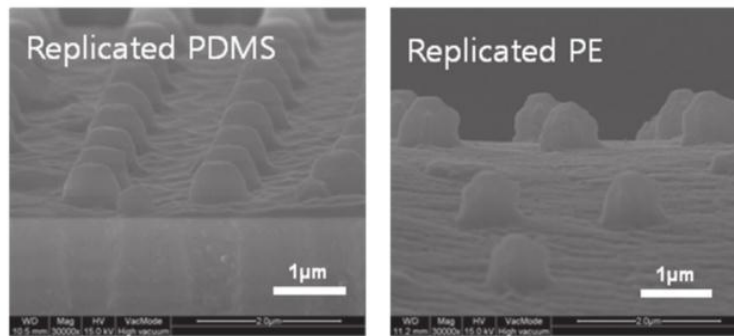


Figure 1.9 Replicated PDMS and PE nanoprotusions [37].

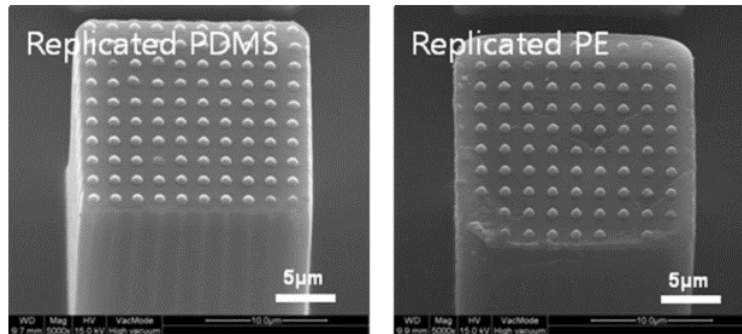


Figure 1.10 Replicated PDMS and PE nano-microstructures [37].

In another study of the authors [38], two nickel micromolds with pillar- and pore-type micro-structures were fabricated on 1 mm thick PMMA. The optimum ultrasonic time

was found as 2 s and 2.5 s for the pillar- and pore-type micromolds, respectively. The pillar-type micromold patterns were $53.7\text{ }\mu\text{m}$ high and $70.5\text{ }\mu\text{m}$ width, whereas, pore-type micromolds were $53.8\text{ }\mu\text{m}$ high and $69\text{ }\mu\text{m}$ width. The replication rate of pillar-type micromolds (figure 1.11) on PMMA were 99% in width and 97% in height. On the other hand, the replication rates of pore-type micromolds (figure 1.12) are found 99% in width and 98% in height.

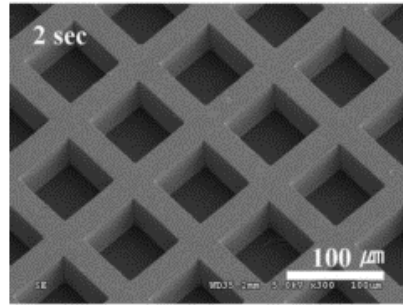


Figure 1.11 SEM of the pillar-type micromold replicated on PMMA [38].

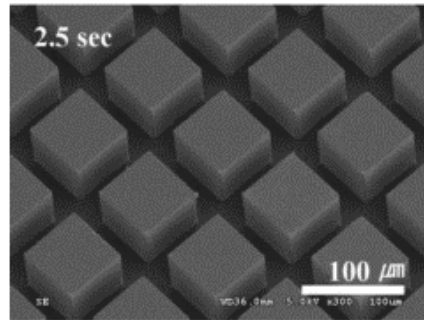


Figure 1.12 SEM of the pore-type micromold replicated on PMMA [38].

Tan et al. [39] simulated the material flow pattern and the temperature distribution during the process by using Deform2D software to explain the UE process physics.

Resemblance between numerically found flow patterns and experimental embossed features were reported.

Jung et al. [40] numerically investigated the heating mechanism of UE (using an E-shaped mask and AA1050 micropatterned mold) in embossing of 300 μm PET film substrate at 0.4 MPa embossing pressure and 1 s time settings. Similar temperature trends were found between the numerical findings (FEA) and experimental results. Different embossing times were tested experimentally to find the optimum time setting.

1.3 Objective of Thesis

As mentioned in Chapter 1.2, the UE studies were concentrated on production of miniature electronic devices [25, 27, 29] and microfluidic devices with microchannels for biomedical applications [28, 41]. In the literature, the published works are generally on the effects of UE parameters (vibration amplitude [33, 36, 42, 43], vibration frequency [36], temperature of substrate and mold [32, 33, 42, 44, 45], processing time [22, 33, 36, 40, 42-48], force [22, 33, 36, 42-48], substrate material [26, 31, 36, 38], substrate geometry [33, 36], mold pattern [30, 33, 35-38], mold production techniques [21]) on replicated channels and other forms as well as optimization of the process variables for having better replication rates and surface characteristics. Although there are some other works on thermal characteristics and temperature measurements of the UE process [33, 34, 40, 42, 48], there are no comprehensive works on investigation of the process principles (physics) underlying using numerical modelling and experimental validation.

Very limited number of studies, which are performed at the Aachen University, on thin substrates (foils), on microfluidic device applications of UE embossed chips are available in the literature (micro thermal flow sensor [28], micro T-mixer [41], micro reactor [49], micro heat exchanger [50], micro pump [51]).

The literature survey revealed the use of polymer embossed substrates thicknesses in between 125 and 250 μm for fabrication of some electronic devices and components rather than microfluidic channels. The maximum thickness of substrate used in UE is 2 mm for double sided replication of mold patterns [33]. Although, thick substrates

above 2 mm are usable in microfluidic channel applications, they have not been used in published UE studies since ultrasonic energy is dispersed in the massive substrate body causing embossing difficulties.

The thesis studies will cover the following issues to fill the gap in the literature;

- Experimental and numerical study on hot embossing (HE) (for better understanding the principles of UE),
- finite element modelling of the UE process (deformation of the substrate and the temperature distribution on the substrate and the mold) to understand and visualize the mechanism of the process,
- performing experiments (aluminum mold will be used on PMMA embossing) and temperature measurements during the process to observe the behavior of the substrate during the process,
- material tests to understand embossed PMMA material property changes,
- comparison the experimental and theoretical findings,
- use of thick substrates (3 mm thick) in both modelling and experimental phases of the study,
- design, fabrication, sealing and use of an UE embossed droplet based microfluidic chip to show the suitability of the UE process in microfluidic applications (mold pattern is formed by micromilling).

1.4 Organization of the Thesis

In this chapter (Chapter 1), brief information about widely used plastic microfabrication techniques such as PDMS molding, micromilling, HE, injection molding and UE methods are given. In this thesis, UE is introduced as a suitable technique to fabricate thermoplastic microfluidic devices considering its' short fabrication cycle time per chip and low cost of the equipment. Additionally, a detailed review of UE process is presented.

In Chapter 2, the process principles and literature survey of HE is introduced in detail since the basic mechanism underlying the embossing action is valid for both HE and UE techniques. The numerical and experimental analysis of HE for equally spaced protrusions are presented. The most affective parameters on HE performance outputs

are presented and discussed by using ANOVA. A microreactor is fabricated for demonstrating the microfluidic device fabrication capabilities of the HE. The procedure to seal the chip with solvent assisted thermo-compressive bonding is given.

In Chapter 3, the mechanism of UE is investigated by means of numerical analysis and experiments. In the experiments, micromilled molds are used to ultrasonically emboss the patterns on PMMA substrates. The process affected zone (PAZ) is investigated by using close-up photographs, thermal camera images, developed finite element model and material characterisation tests. The findings are compared and discussed. Dynamic transmitted force to PMMA during the UE process is measured. The future studies are recommended.

Chapter 4 presents the detailed numerical analysis, design and fabrication procedures of a droplet generator device for bioprinting purpose as a LOC application. The initial test results of the fabricated droplet generator for bioprinting has proven the suitability of the UE process for chip embossing and micromilling technique for molds production.

The last chapter finalizes the thesis with concluding remarks and recommendations for future studies.

CHAPTER 2

HOT EMBOSSING (HE)

The mechanism of HE is based on overall heating and deformation of substrate under high temperature and pressure settings. On the other hand, the UE process mechanism, which is the main focus of this study, based on local heating and deformation of substrate at a very short time interval. In order to establish the mechanism of UE process, first the HE process variables and their effects on performance outputs should be understood. So, in this chapter firstly a brief review of HE process was introduced. Afterwards, the conducted numerical and experimental studies in the scope of the thesis were given.

HE process is known for more than a decade in microfluidic device fabrication [52, 53]. Yet, there are limited number of comprehensive published work in the field on effects of process parameters on fabrication and performance of HE microfluidic devices. One of the study in the field revealed that the embossing temperature had an utmost importance on the replication rate of the microfluidic device channels made of polystyrene, PMMA and PC substrates. It was shown that $T_g + 40^\circ\text{C}$ gave the best replication rates and mold size had no significant effect on the replication accuracy [54]. In one of study [55] on optimization of HE temperature and force to replicate 50–100 μm features on PMMA, whereas limited number of settings were tested, it was revealed that 100°C embossing temperature and 10 kN force at 5 min HE time were suitable settings for best replication rates. The effect of mold temperature ($180\text{--}220^\circ\text{C}$) and pressure ($10\text{--}30\text{ kgf/cm}^2$) on replication rate of patterns for PC substrate was investigated in reference [56]. At 210°C , the replication rate was found 97.5% for 20 kgf/cm^2 pressure. In [57], the effects of temperature ($150\text{--}200^\circ\text{C}$), force (300–1500 N), and mold dimensions (5–100 μm) on PMMA relaxation after demolding revealed the importance of reduced temperature and pattern size. In other two works [58, 59], at 170°C temperature and 55 kgf force settings, perfect replications (99%) on PMMA for Fresnel lenses were obtained. Various temperature ($100\text{--}125^\circ\text{C}$),

pressure (900–3600 kPa), and time (1–4 min) settings were tested to improve channels replication rate on PMMA substrate in reference [60]. The study revealed the importance of temperature on replication rate whereas 125°C, 3200 kPa, and 6 min settings were found for the best replication rates. In Konstantinou et al. study [61], the best replications were obtained at 170°C, 26.7 kN, and 6 min settings for PMMA and COC substrates. He et al. [62] used 100–300 N (low force settings) to obtain acceptable replications on PMMA substrate whereas 300 N, 150°C and 0.5 h yielded the best replications. Jena et al. [63] used silicon, epoxy, and COC molds to investigate the filling of COC substrate for varying temperature ($T_g + (2-22)^\circ\text{C}$), force (1–3 kN), and time (1–5 min) settings. The best replication rates were obtained for silicon mold at 80°C. Lin et al. [64] obtained accurate replications on PMMA close to the center of the mold. Liu et al. [65] study revealed reduction of “swallowtails” (typical embossing defects appearing as unfilled corners at the roots of the protrusions on the mold) with increasing embossing time.

2.1 Working Principle

In HE, the heater plates are heated above T_g of substrate. The mold is placed on the heater plate and heated up to T_g . Afterwards, the substrate is placed on the heated mold (figure 2.1(a)). Substrate is embossed under a specific force for a certain time (figure 2.1(b)). After cooling, the substrate is demolded (figure 2.1(c)) to release the chip (figure 2.1(d)) [66].

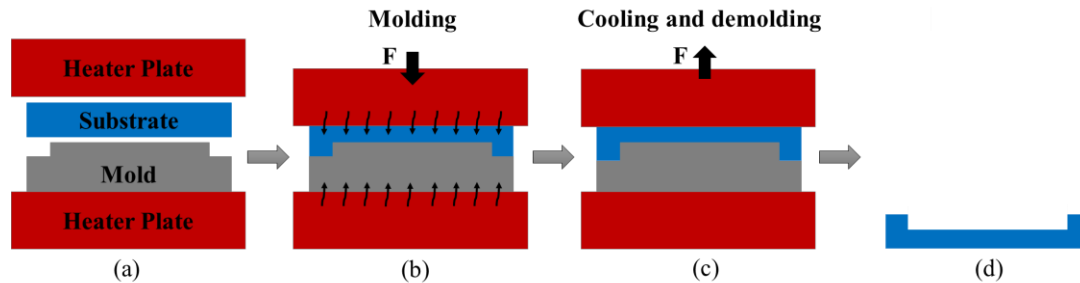


Figure 2.1 Stages of HE, (a) substrate placement, (b) compression, (c) cooling and demolding, (d) embossed substrate [66].

2.2 Numerical Analysis

In this thesis, finite element analyses were conducted via ABAQUS software. The aluminum mold and the upper heater plate were modeled as rigid, while the PMMA was modeled as a deformable body by eight-node linear brick elements. The upper heater plate moved toward the PMMA with 5 kN constant force. The mold was held stationary at the bottom of the substrate. The substrate was free to deform in all directions. Flow stress of PMMA was taken constant (20 MPa) until 0.9 strain at 105°C. Convergence tests revealed insignificant variation in the analysis results for more than 661250 PMMA elements.

The replications on PMMA on the right half of the mold were investigated (figure 2.2(a)) [66]. The right skewness (R1, R2 and R3) increases with increasing distance from the center of the substrate.

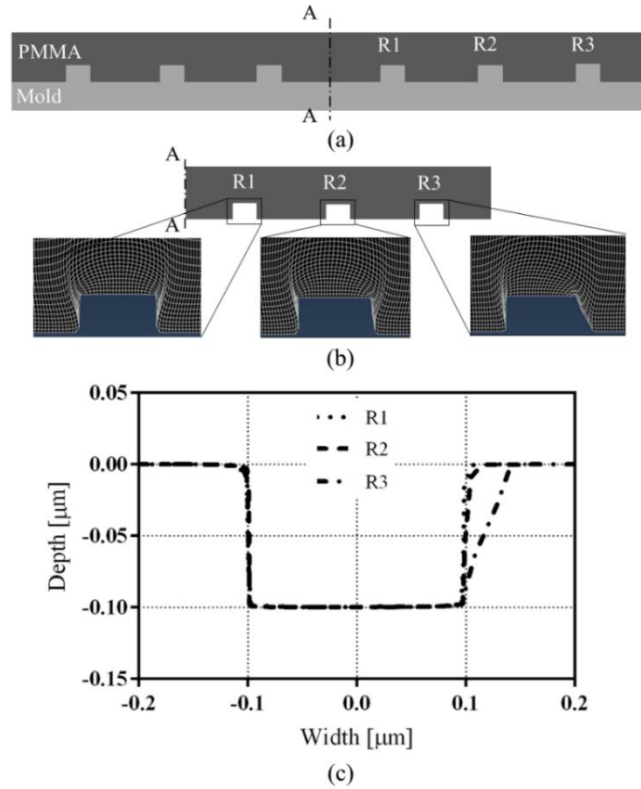


Figure 2. 2 (a) Mold and substrate; (b) right half of the substrate; (c) comparison of R1, R2, and R3 profiles [66].

Full size molds with single protrusion either located on the left, the center, or the right of the mold were considered to understand effects of location and density of protrusions on skewness (figures 2.3(a)–(c)). The replicated profiles on the left and right were fully symmetric since the substrate material flowed from center to sides, whereas the center one had no skewness, as expected (figure 2.3(d)) [66].

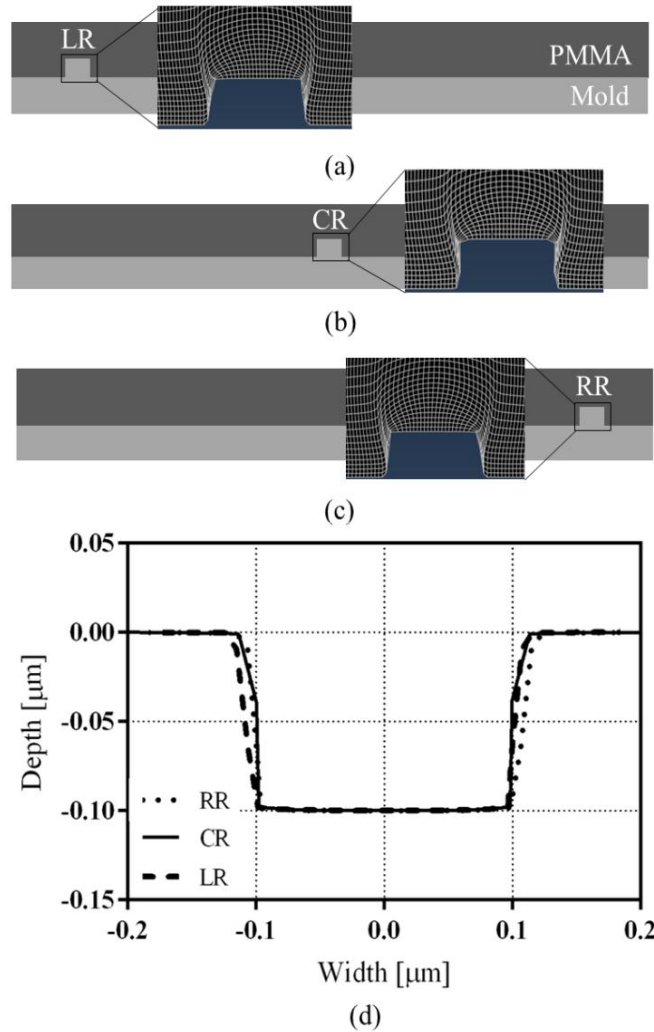


Figure 2. 3 Single replication cases: (a) on the left (LR), (b) at the center (CR), (c) on the right (RR).
(d) Comparison of LR, CR, and RR profiles [66].

Moreover, the skewness analyses performed by using six protrusions (figure 2.2(a)) and a single protrusion (figure 2.3(c)) demonstrated higher skewness for higher-density protrusions (figure 2.4). Higher shear stress computed at the mold–substrate and plate–substrate interfaces than that at the core of the substrate revealed the resistance to flow caused by the interface surface conditions. Higher quality surface textures of the mold and the plate reduced the interface flow resistance, thus enabling better filling at the near root of the protrusions with respect to the material flow direction. On the other hand, skewness at the far root was inevitable [66].

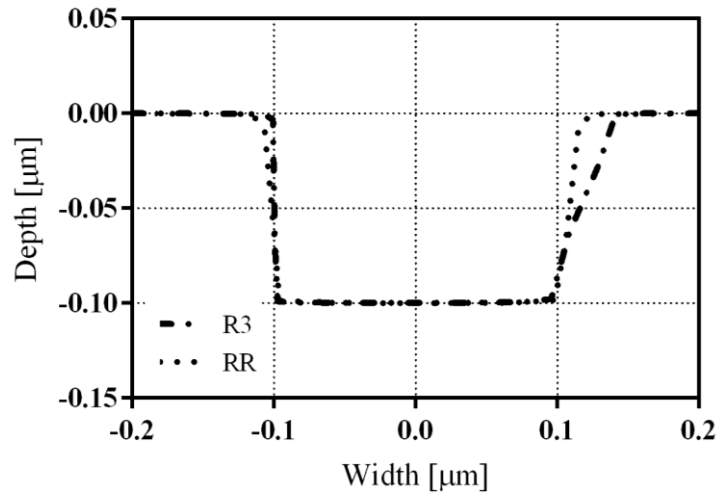


Figure 2.4 Comparison of RR and R3 profiles [66].

2.3 Experimental Work

In HE experiments, a hydraulic press with 100 kN capacity was used. Two resistive heaters (each 300 W) were used to heat the plates (figure 2.5(a)) with $\pm 1^\circ\text{C}$ accuracy. The mold was placed on the lower heater plate and PMMA substrate was located on the mold. The substrate was heated via the upper heater plate and the mold. Embossing force (F) was applied by lowering the upper heater plate.

The mold used in the experiments had a micro-reactor chip form having a serpentine (with 400 μm width channels) and straight protrusions (at five different widths) (Table

2.1). The patterns were micromilled on a $50 \times 20 \times 10$ mm AA7075 aluminum using end mills with 1 mm dia. (for roughing) and 0.2 mm dia. (for wall finishing) (figure 2.5(c)). The mold was fixed to the machine table by means of double side sticky tape. Zeros of milling cutters were set by the help of a small microscope. The micromilling was conducted by a desktop milling machine (ProLIGHT 1000 Machining Center, Light Machines Corp., Manchester, NH, USA) at 3500 rev/min speed and 100 mm/min feed. The mold embossed the features on $50 \times 25 \times 3$ mm PMMA substrate (figure 2.5(b)) [66].

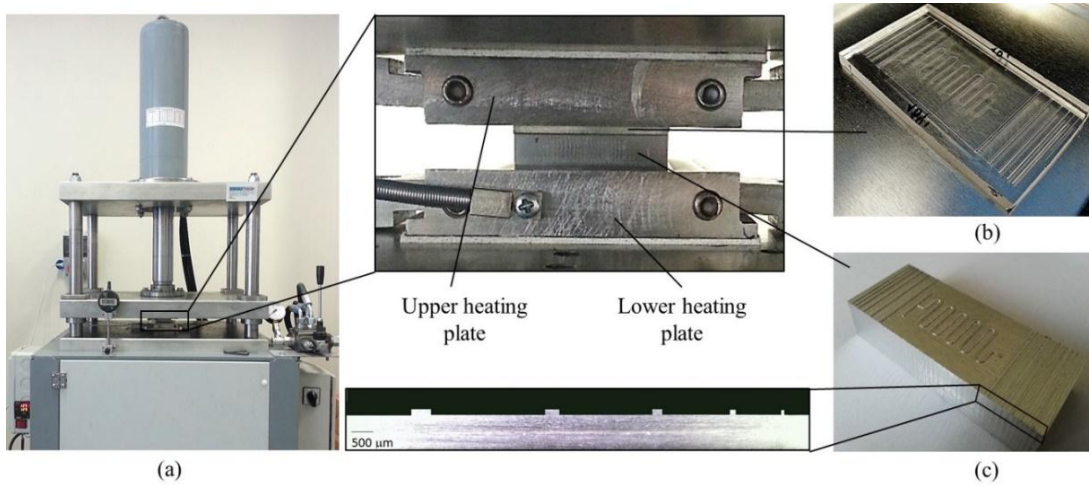


Figure 2.5 (a) HE press and heating plates, (b) embossed chip, (c) fabricated mold and its' protrusions [66].

The initial tests demonstrated embossing of well-replicated features at 110°C , 9.5 kN and 7 min settings. For the experiments, three levels of the parameters (temperature, force and time) were selected based on the initial tests (Table 2.2). Experiments were repeated four times and averages of the measurements (widths and depths) were used.

Table 2.1 Dimensions of mold straight protrusions. The difference between nominal and actual dimensions is due to the deflection and run-out of the milling cutters and resolution of the machine tool [66].

Nominal width [μm]	Nominal depth [μm]	Actual width [μm]	Actual depth [μm]
100	100	56	111
200	100	105	116
300	100	216	120
400	100	310	120
500	100	436	122

Channel profiles (figures 2.6(f)–(j)) were captured by a camera mounted on a microscope. The images were processed by ImageJ [67] commercial software to determine the dimensions of replicated channels and the mold patterns. The width replication rate (r_w) and depth replication rate (r_d) are described as [66];

$$r_w = 100 \left(\frac{w_c}{w_m} \right) \quad (2.1)$$

$$r_d = 100 \left(\frac{d_c}{d_m} \right) \quad (2.2)$$

Here, w_c and d_c are the width and the depth of the replicated channel, while w_m and d_m are the width and the depth of mold patterns, respectively. The w_c and d_c values were measured as the average width and the average depth across the channel as illustrated in figure 2.6(f) [66].

Two key conclusions can be drawn from the replicated channels profiles shown in Figures 2.6(k)–(o); a) the bottom width of the replicated channels were almost the same with that of the mold, b) the upper left and right corners were rounded (“swallowtail” defect [68]).

Table 2.2 HE parameters used in the experiments [66].

Experiment	Temperature (°C)	Force (kN)	Time (min)
1	100	8	6
2	100	9	7
3	100	10	8
4	105	8	6
5	105	9	7
6	105	10	8
7	115	8	6
8	115	9	7
9	115	10	8

The results also revealed the minimization of swallowtail defect as well as enhanced r_w (approaches 100% (figure 2.7(a)) by increasing temperature. Figure 2.7(a) also indicated significantly higher replicated width than that of mold especially for relatively low-width-protrusions (for 56 μm wide features r_w reached 200%). In wide features and relatively high HE temperatures, r_w reached to 100%. However, replicated depth was insensitive to temperature (r_d remained at about 100%) (figure 2.7(b)) [66].

Examination of the profiles (figures 2.6(f)-(j)) revealed the skewness of side walls of the replicated channels to the left side of the substrate (figures 2.6(k)-(o)) instead of being symmetric. It should be noted that the profiles shown in figures 2.6(a)-(o) represent the replicated channels located on the left side of the substrate (figure 2.6(p)). It was shown that the skewness formation was affected by the location of the pattern on the mold and the direction of the material flow during HE. A reasonable explanation was that the material at the center of the substrate started flowing through the sides of the substrate as the protrusions on the mold penetrated into the substrate during embossing. However, the mold protrusions resisted the material flow and hindered filling of the cavities at the far root of the protrusions with respect to the material flow direction [66].

The observation of skewness increased with increasing distance between the protrusion and the center of the substrate also supported this finding. Replicated channels on the far left of the substrate (figure 2.6(k)) showed significantly higher skewness than the channels close to the center of the substrate (figure 2.6(n)). Another supporting observation was the skewness of replicated channels on the right side of the substrate to the right side of the substrate, opposite to the channels on the left side [66].

The FEA results (figures 2.2, 2.3 and 2.4) were in agreement with the experimental findings (figure 2.6) as the right skewness increased with increasing distance from the center of the substrate (figure 2.2(b)-(c)) [66]. The author believes that the skewness problem can be resolved by restricting the material flow on the sides by using a closed mold. Moreover, figures 2.6(k)-(o) indicated that the skewness defect could be partially resolved by higher the embossing temperatures [66].

Figures 2.7(a)-(b) revealed enhancement of replication rates by increasing the temperature. Better replication rates were attained at 115°C embossing temperature. This result implied that PMMA substrate significantly softens at this temperature by enhancing workability of the material [69]. The softening behavior of the PMMA substrate was tested using a type-D Shore durometer [66]. The test yielded sharply decreasing hardness at 110°C (figure 2.8(a)), which justified the embossing tests findings.

Moreover, differential scanning calorimeter (DSC) analysis revealed 107°C glass transition temperature for the substrate (figure 2.8(b)). r_w for each feature at different force and time settings are shown in Figure 2.7(c). r_d was not investigated for the remaining cases since r_d unchanged with varying settings (figure 2.7(b)). Figure 2.8(c) revealed enhancing r_w with increasing force and time especially in relatively narrow channels. This result was consistent with the findings reported in [70]. However, the improvement in r_w for channels wider than 200 μm was insignificant. In this study, the best HE replication rates were obtained at 115°C, 10 kN and 8 min settings [66].

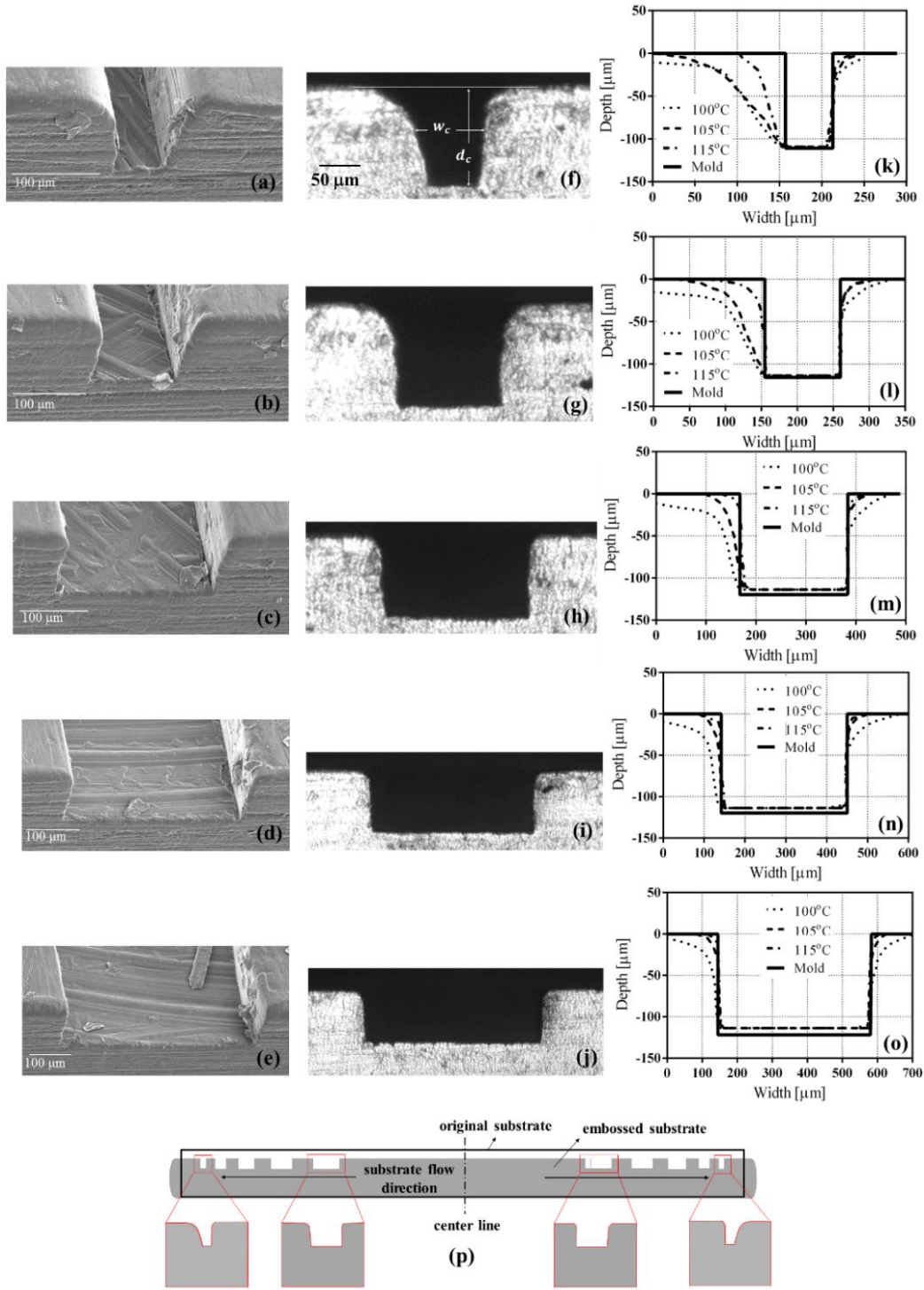


Figure 2.6 (a)-(e) SEM images of the replicated channels embossed at 115°C, 8 kN, and 6 min settings by using 56, 105, 216, 310, and 436 μm protrusions. (f)–(j) microscope views of channels. (k)–(o) Channel profile plots for different temperatures (for 8 kN, 6 min) and the same mold width. (p) Illustration of the PMMA substrate [66].

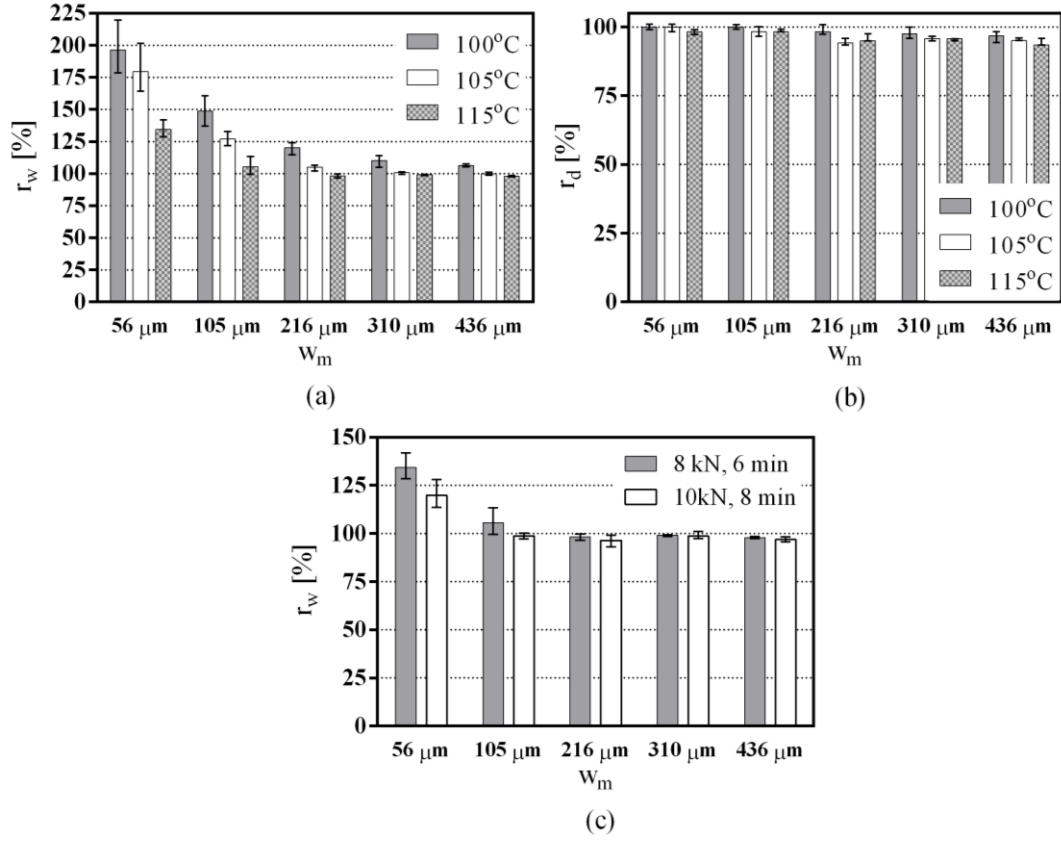


Figure 2.7 (a) r_w and (b) r_d for different temperatures and mold feature widths (embossing force and time are 8 kN and 6 min, respectively). (c) r_w values at 115°C for different force and time settings [66].

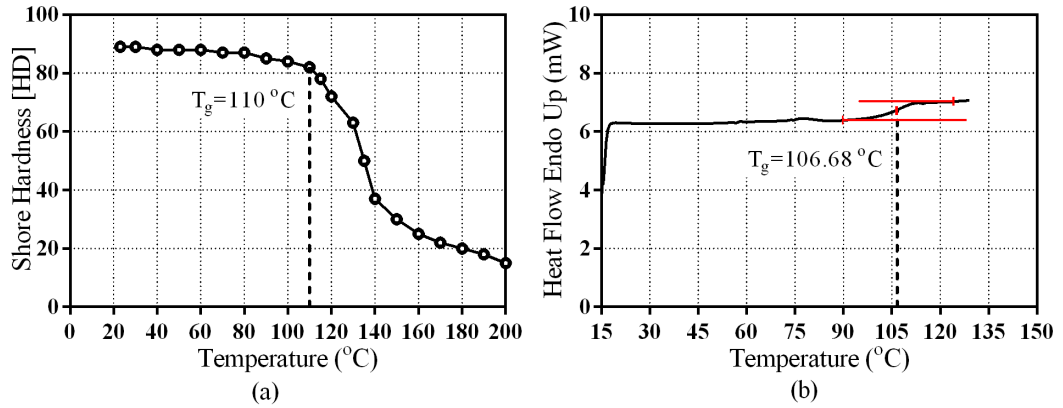


Figure 2.8 (a) Shore-D hardness test [66], (b) DSC analysis of PMMA substrate.

The analysis of variance (ANOVA) and F-test [71] were used to obtain the relative importance of process parameters on replication characteristics. For the width of replicated channels, the ANOVA yielded low error values (3.3% max.) for all experiments. Since the widths of the replications were higher than the molds in HE, the LB (lower the better) criterion was chosen for better width replication. The signal/noise (S/N) diagrams for 105 μm mold pattern width at varying process parameters (figure 2.9) showed that the greatest change in S/N ratio was obtained by changing the temperature and highest S/N ratio was obtained at 115°C, 10 kN and 8 min (optimum settings) [66]. The results pointed out embossing temperature as the most important parameter in replication rates.

Temperature, force and time were 85.3%, 8.2% and 5.6% effective on replication width respectively with 95% confidence level for 105 μm mold feature. ANOVA and F-test revealed the heavy affect (85.3-95.9%) of varying temperature on width of the replicated channels. The effect of force (less than 8.2% contribution) and time (less than 5.6% contribution) on replicated channel widths were relatively insignificant [66].

2.4 Demonstration of Hot Embossing

A $50 \times 20 \times 10$ mm mold (aluminum 7075) was micromilled in 45 minutes (figure 2.10(a)). The $50 \times 25 \times 3$ mm PMMA substrates were embossed by using the mold at 115°C, 10 kN and 8 min (optimum settings for the best replication rates (Chapter 2.3)). Then, the inlet and outlet of embossed PMMA were drilled (figure 2.10(b)). A number of tests were conducted to find the suitable settings for a successful bonding in thermo-compressive bonding [66]. Generally, thermo-compressive bonding was performed above T_g (110°C for PMMA) [72] in sealing thermoplastic microfluidic devices. However, this high temperature frequently led to some structural defects due to thermal stresses [66]. In this study, a 3 mm thick blank PMMA and the embossed-drilled PMMA were exposed to chloroform vapor at room temperature prior to bonding process to reduce the bonding temperature as suggested in [73, 74] (figure 2.10(c)) [66]. Chloroform vapor treatment also removed partially milling cutter signs from the embossed channel surfaces.

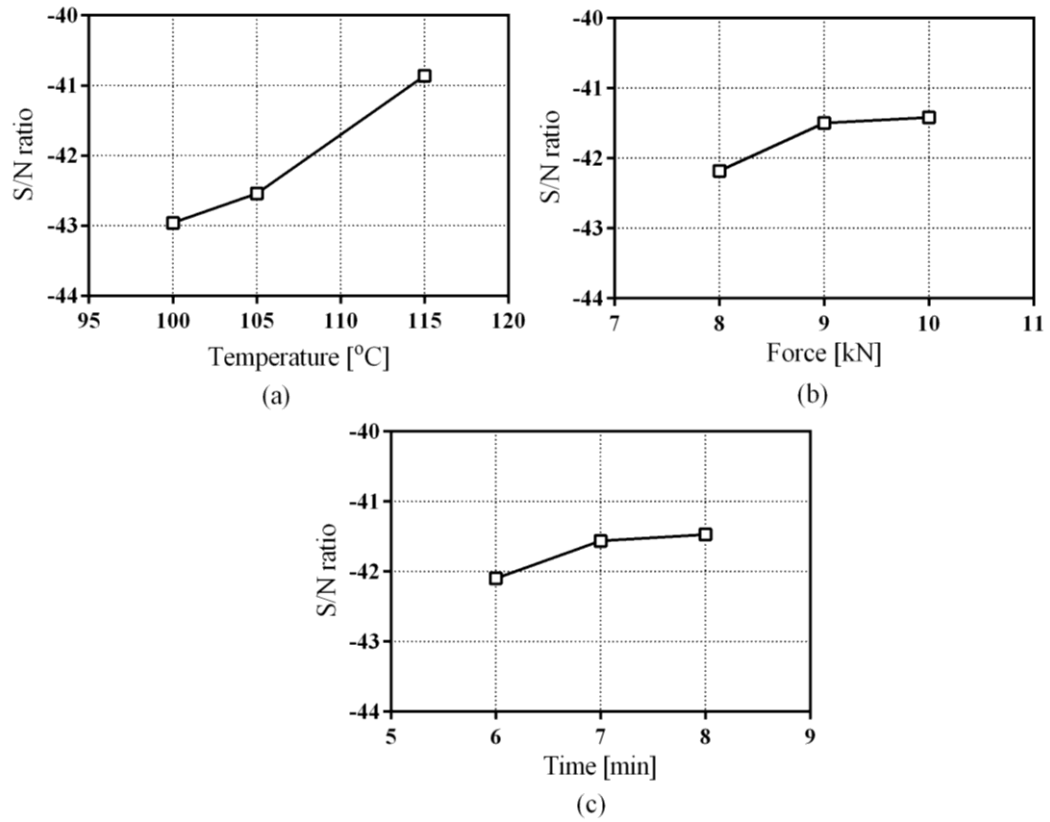


Figure 2.9 S/N ratios for different process parameters for 105 μm mold feature width [66].

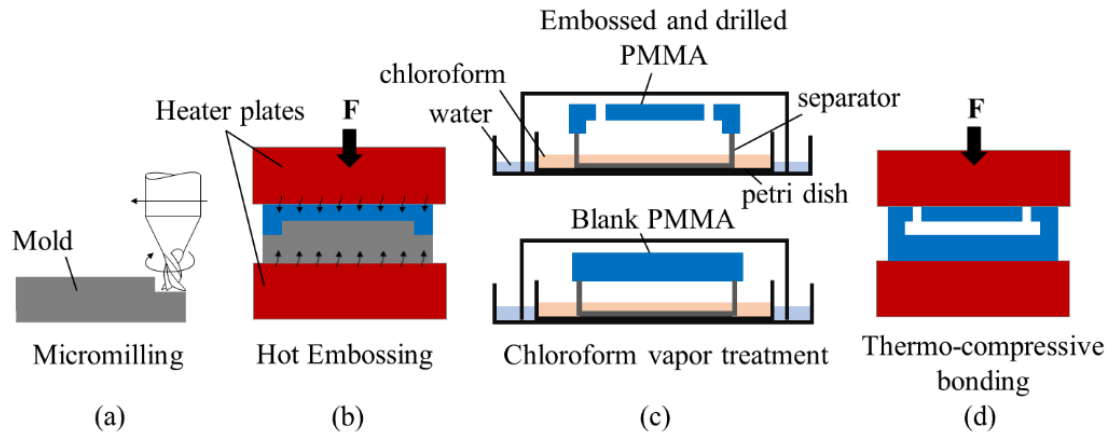


Figure 2.10 (a)-(d) Fabrication of the microfluidic chips.

Successful sealings were obtained at 5.5 kN bonding force, 85°C bonding temperature, 3 min chloroform treatment and 3 min bonding time settings (figure 2.10(d)) [66]. Dyed water dispensed in the replicated micro reactor (figure 2.11) showed no leakage through the edges of the microchannels [66].

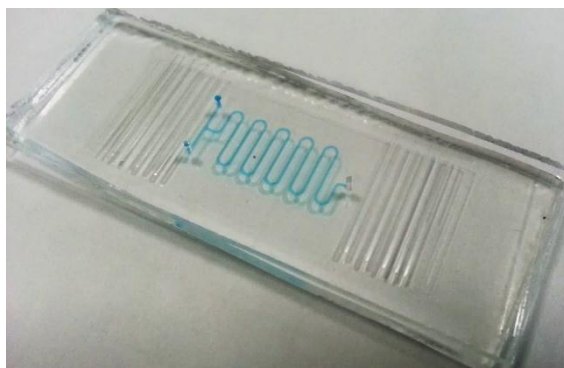


Figure 2.11 A bonded microfluidic chip after dispensing dyed water for leakage test [66].

2.5 Discussion and Conclusion

In this part of the study, the replication rates (r_w and r_d) of hot embossed channels at varying widths (56-436 μm) on PMMA substrates for varying embossing temperature, force and time were investigated experimentally.

Increasing the embossing temperature enhanced the r_w , improved significantly the filling of the cavities at the roots of the protrusions and eliminated the swallowtail defects. The best width and depth replications rates were obtained at 115°C. The r_w was 130% of the 56 μm width mold protrusion. Embossing of channels wider than 200 μm yielded perfect replications even at 100°C (the lowest temperature setting). The elevated temperature beyond 115°C resulted in excessive lateral deformation as well as thinning of the substrate [66].

The results of ANOVA revealed the importance of temperature on r_w , whereas the impact of force and time together were relatively insignificant [66].

Especially at low embossing temperatures the replicated channels on the left of the mold were skewed to left whereas the ones on the right were skewed to right. The skewness defect) was attributed to the material flow characteristics during embossing as well as the locations of the protrusions on the mold. The FEA findings about skewness formations were in agreement with the experimental results. In addition to that the FEA revealed the increasing skewness with the increasing protrusions density [66].

In this study, the settings of 85°C temperature, 5.5 kN force, 3 min holding time and 3 min chloroform vapor time were recommended to have best sealings of replicated chips by solvent-vapor assisted thermo-compressive bonding [66].

CHAPTER 3

ULTRASONIC EMBOSSING (UE)

This chapter presents the principles of UE technique in detail, the results of numerical and experimental investigations and discussion of the findings.

3.1 Working Principle

In UE, a substrate is placed under the mold with protruding pattern (figure 3.1(a)). A sonotrode (horn) vibrating at ultrasonic frequency (above 15 kHz) is pressed to the mold onto the substrate (figure 3.1(b)-(c)) generating heat where protruding mold pattern is in contact to the substrate. At this stage of the process, frictional heat caused by ultrasonic vibration locally melts the substrate surface which is in contact with the mold protruding pattern [75, 76]. After cooling (some hundred milliseconds are enough [76]) of the polymer, the sonotrode is moved up (figure 3.1(d)) and substrate is removed from the tool (figure 3.1(e)). While HE requires complete melting of the substrate, the directed energy input and locally restricted melting achieved by UE lead to reduced shrinkage and heat distortion [75]. The geometrical (shape) quality of the embossed structure depends on the quality of the mold [77].

PA (polyamide), PP, MABS (methyl methacrylate acrylonitrile butadiene styrene copolymer), PC, PS, PVDF (polyvinylidene fluoride), PEEK (polyether ether ketone), HDPE (high density polyethylene), LDPE (low density polyethylene), PET, SAN (styrene–acrylonitrile copolymer), PMMA, PVC and PETG polymers are suitable substrate materials for UE [76, 78].

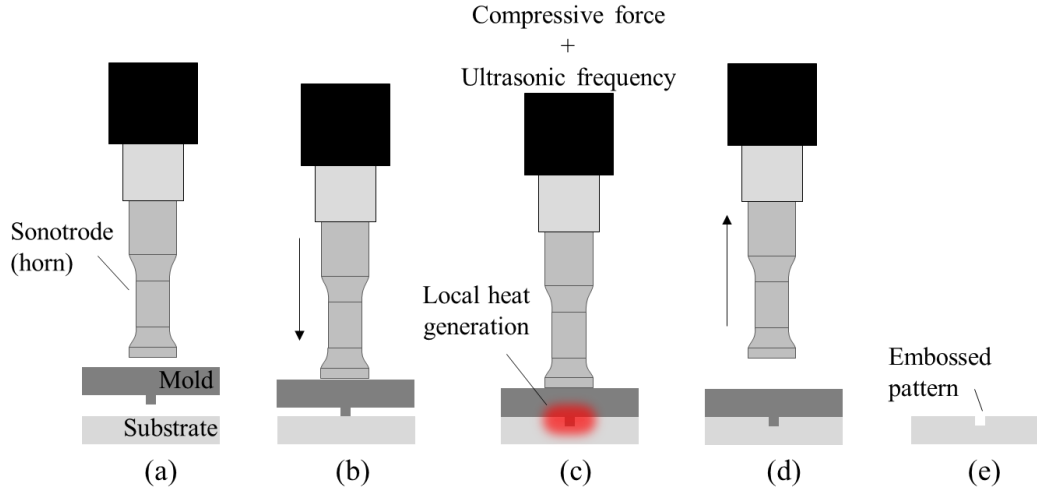


Figure 3.1 The stages of UE process.

3.2 Numerical Analysis

A FE model was built to analyze the UE process by using ABAQUS. In the model, a simple protrusion pattern (200 μm width and 150 μm height) was embossed on to the substrate surface to replicate a straight microchannel. The deformations along the length of the channel were ignored since the channel length was much higher than the width and the height of the microchannel. So, a 2D model was adequate to simulate the process. In order to reduce the computing time, only the half of the mold and the substrate were used in the analysis. The x-symmetric boundary condition was described for the substrate at the symmetry line. The mold and the substrate sizes (2 mm width and 1.5 mm height for the both (figure 3.2(a))) were so selected that there was no significant substrate flow and temperature variations at the outer boundaries (i.e. remaining volume). Zero lateral displacement was described for substrate since the holder constrained its lateral motion. All rotational deformations in the substrate body are allowed.

The mold and the substrate were considered as deformable bodies in the analysis. Four-node plane stress thermally coupled quadrilateral element (CPS4RT) was used in meshing the mold and substrate. Meshing was automatically re-generated (with 100000 frequency) at the regions where large deformations were expected to prevent

excessive distortion of the elements. Moreover, small elements were used at these regions to analyze the temperature and deformation variations accurately. Mesh dependency tests revealed that a 300 elements (total of mold and substrate (Figure 3.2(b))) was a sufficient number in simulating the process accurately. No significant changes in temperature and deformation analyses were found beyond this number of mesh.

The vibration frequency and the amplitude of the sonotrode were taken as 28 kHz and 10 μm , respectively, for the ultrasonic power source and the sonotrode geometry in use. The vibration of the sonotrode hammers the mold on the substrate causing an intermittent downward motion of the mold. This motion was modelled by superposing a vibrating motion (equal to that of the sonotrode) and a constant downward feed. The frequency and amplitude were input to describe the vibrating motion of mold. In the preliminary tests, a 150 μm deep protrusion was replicated in 2 s. So, the down-feed speed of the mold was taken constant as 75 $\mu\text{m/s}$ in the analysis. The motion of the mold is modelled via a custom subroutine VUAMP [79]. The PMMA was held stationary at its bottom surface. The mold and substrate material properties given in Table 3.1 and Table 3.2 were used in the FEM. In precise process modelling, the true stress-true strain relations of PMMA at different temperatures are required. Since the strain rate is high in UE, the highest strain rate data available in the literature (at 1 s^{-1} for 15°C - 115°C (figure 3.2(c))) was input to the model. The initial temperature of mold and substrate were given as 25°C .

In order to reduce the number of numerical analysis iterations, the initial settings of UE to be used in the analysis (the mold pattern dimensions, the feed speed of the mold, embossing force, embossing time) were obtained from preliminary UE tests. So, the numerical analysis provided more accurate UE settings for better embossed channel replications with less effort, which will be used in the experimental phase of this study.

Simulations were run for 5 s embossing time, t_e (at 25°C initial temperature). For the computer used in the analysis (Intel Core i3-6100/3.7 GHz microprocessor with 12 GB RAM) the processing for the solution took 51.5 h CPU time.

Table 3.1 PMMA material properties [80]. Thermal conductivity was taken as 0.18 W/m.K irrespective of the temperature.

Temperature (°C)	Density (kg/m ³)	Young Modulus (MPa)
15	1190	6000
30	1185	5750
60	1170	5000
90	1155	4000
100	1155	3500

Table 3.2 Material properties of the mold (aluminum 7075).

Density (kg/m ³)	Young Modulus (MPa)	Poisson's Ratio	Thermal Conductivity (W/m.K)
2800	8000	0.33	130

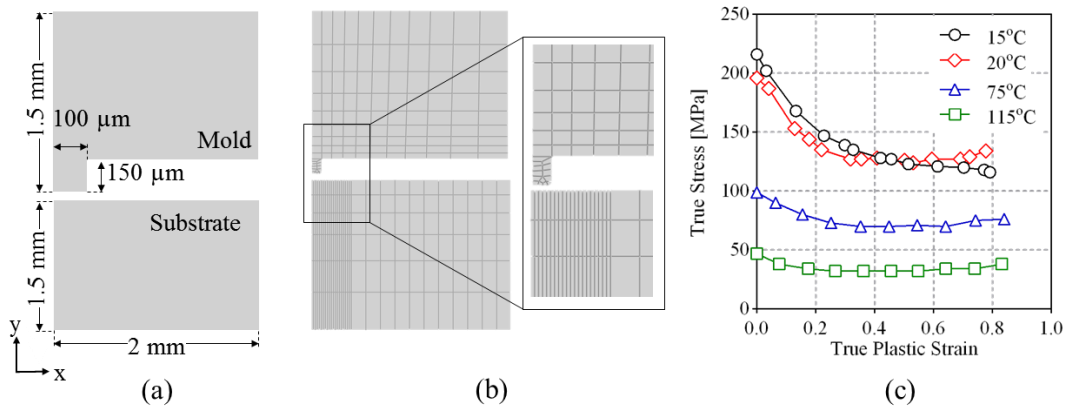


Figure 3.2 Schematic view of (a) mold and PMMA, (b) meshing. (c) True stress-plastic strain of PMMA (at 1 s⁻¹ strain rate) with varying temperature [81].

Simulation results indicated the highest temperature at the tip of the mold protrusion (figure 3.3(a)). In the first phase (in the first 2 s) of embossing the mold hammered the substrate at ultrasonic mode causing plastic deformation (plastic work) and heat generation. The heat generated was carried away via the mold and the substrate. Lower thermal conductivity of the substrate (0.18 W/m.K for PMMA) than the mold (130 W/m.K for aluminum) caused higher temperatures at the mold side. At this time

interval, plastic work done by hammering was the main mode of heat generation whereas the friction between mold and substrate was also effective, but at a lower rate. After the full embossment of the mold protrusion on the substrate (no down feed of the mold after 2 s), only the friction between the mold and channel walls was effective on heat generation. The mold temperature at the tip of the protrusion decreased slightly for a while right after 2 s due to rapid dissipation of heat through the mold. After a short while, the mold and the substrate temperatures were increased since the wall friction effect became dominant in heat generation. Temperature change at the substrate for the first 2 s was validated by increased equivalent plastic strain and von Mises stress (figure 3.3(b)-(c)). Since hammering stopped right after 2 s, the equivalent plastic strain and von Mises stress decreased slightly for a while. Afterwards, they remained constant throughout the remaining cycle. The softening of the substrate resulted in even stress distribution after the first 2 s (figure 3.3(c)). It is noteworthy that von Mises stress up to 70 MPa was observed at the bottom edge of the embossed channels (figure 3.3(c)). This high stress level likely caused crack formations observed at the bottom of the channels since fracture strength of the substrate is much less than 70 MPa at above 25°C [82]. The crack formation was also attributed to stress concentrations at the bottom edges due to considerable temperature difference between bottom and wall of the substrate (figure 3.3(a))

The highest substrate temperature was at the close vicinity of the mold protrusion and the temperature decreased radially outward (figure 3.3). So, the substrate temperature at a certain region exceeded the T_g (107°C for PMMA) at the vicinity of the mold protrusion in UE process. In this study, this region is named as the *process-affected zone (PAZ)*. The PMMA substrates were ultrasonic embossed by using the experimental setup described in “Chapter 3.3 Experimental Work” to validate these findings.

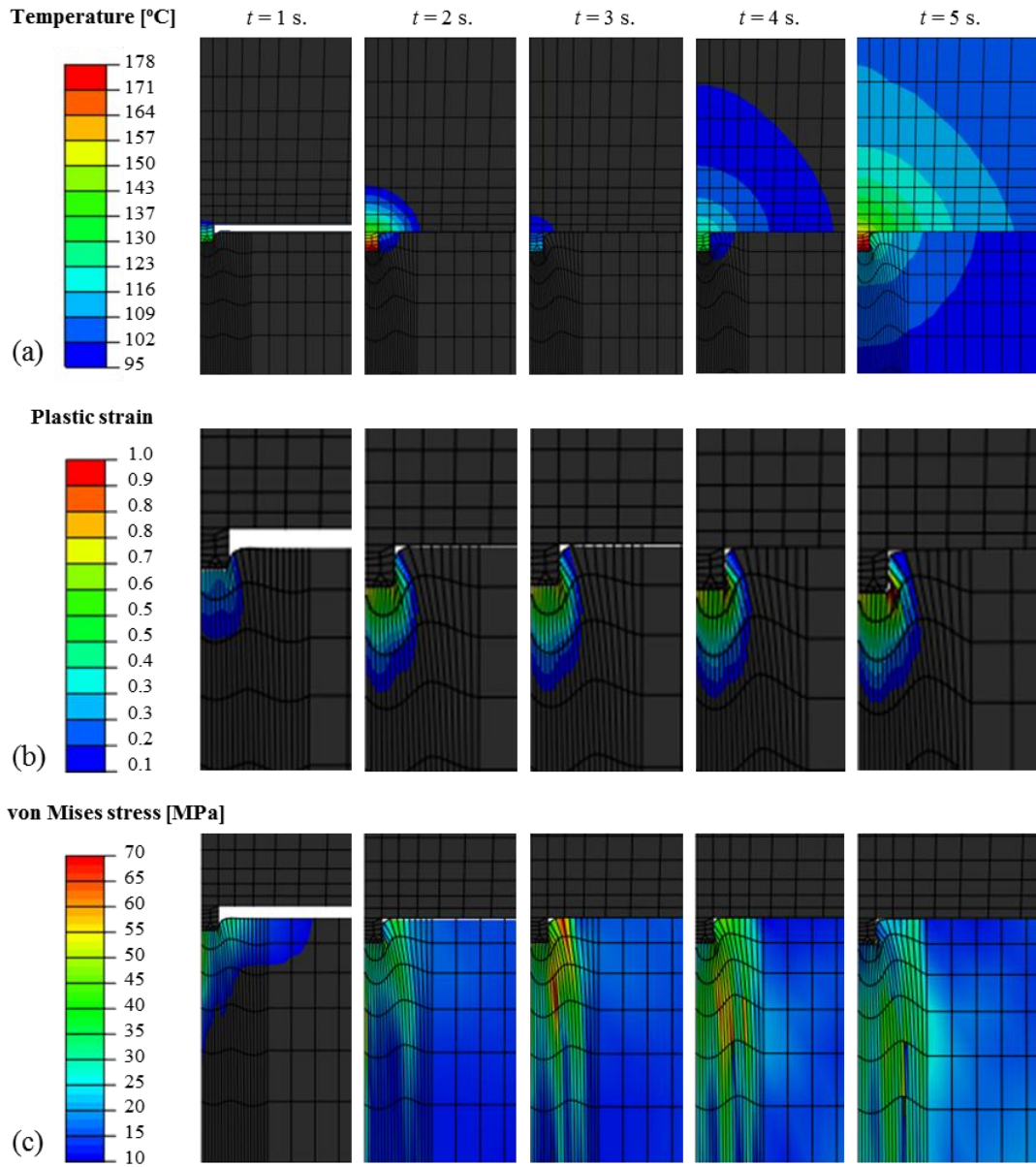


Figure 3.3 (a) Temperature, (b) equivalent plastic strain, and (c) von Mises stress distributions (for 5 s of UE at 25°C).

3.3 Experimental Work

An EGW-2805 type ultrasonic welding head with 28 kHz output frequency and 500 W power was used in the experiments. The head was assembled on a custom-made vertically moving stand plate (figure 3.4). Dead weights were used to load the plate

during the operation. A brass holder which was mounted to the base of the stand was used to place the mold on the substrate. The set-screws which were placed to the holder walls, fixed the substrate and the mold laterally while allowing vertical vibration movement of the mold. A heater plate (400 W) with a thermocouple was attached to the setup to allow UE experiments at elevated temperatures, up to 200°C. An aluminum (AA7075) sonotrode with output of 10 μm amplitude at 28 kHz frequency was manufactured by CNC turning. References [83-86] can be referred for sonotrode design procedures.

The mold had a single straight protrusion (150 μm depth, 200 μm width) pattern which is extended till the edge of the mold to allow visual inspection during the experiments (replication of a straight channel). The 23 x 23 x 3 mm mold was fabricated from aluminum 7075 by micromilling (Chapter 2, section 2.3). 23 x 23 x 3 mm PMMA substrates were used in the tests (Figure 3.4).

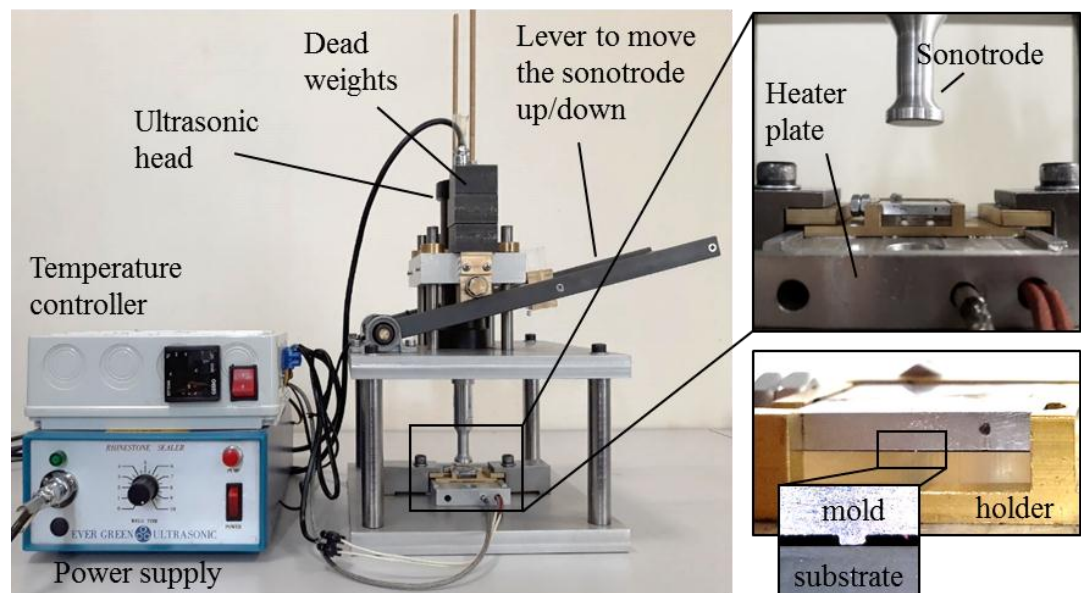


Figure 3.4 Details of the custom-made ultrasonic embossing test set-up.

3.3.1 Process Affected Zone (PAZ)

Experiments were conducted for varying t_e (2, 3, 4, and 5 s) and temperature, T_e (25, 40, 60, 80 and 100°C) settings. The static component of the force, F_{as} (85 N), vibration amplitude (10 μm) and frequency (28 kHz) were kept constant throughout the experiments. The experiments were repeated four times for having reliable results. The PMMA substrate was heated at its bottom and side surfaces by conductive heating for the tests performed at elevated temperatures. During preheating, the mold was placed on top of the PMMA (figure 3.1(b)). When PMMA reached the desired temperature, the sonotrode was moved downward to start the UE process.

After the UE process, the side surface of the substrate, to which the embossed microchannel was perpendicular, were milled to expose a clear section view of the replicated channel. The section view demonstrated a near half-circular region (PAZ) with an elevated top surface (Figure 3.5 (a)). The distance between the channel axis and the end of the elevated surface (approx. the radius of the half-circular region) was named as “characteristic dimension (CD)”. CD values were measured at varying embossing settings of UE using ImageJ software package (open source image processing tool).

The experiments revealed that CD increased with increasing t_e for $T_e=25^\circ\text{C}$ and 100 $^\circ\text{C}$ settings (figure 3.6(a) and 3.6(c)) due to the higher volume of softened PMMA. The increasing T_e up to T_g increased CD (figure 3.6(b)) since UE vibration energy softened more PMMA material next to the embossed channel (figure 3.7). At elevated temperatures beyond T_g , the UE tests couldn't be performed since the vibration of the sonotrode (so the mold) was prevented by the very low stiffness of the hot PMMA substrate. The fringes observed on top of the PAZ (figure 3.6) were spaced more closely at regions next to embossed patterns whereas less closely spaced at distant regions. This was attributed to low flowability of the PMMA, placed distant from the vibrating mold, obstructing the close fringe formation.

The high rate of heat dissipation due to high deformation (strain) rates of the PMMA and friction of the mold-substrate interface (walls) by the vibrating mold couldn't be

rapidly conducted to the PMMA and mold. Therefore, a substantial temperature increase at the embossed zone of the PMMA was observed. So, the zone next to the embossed channel was softened (figure 3.5(a) and figure 3.7). This zone was restricted by stiff PMMA (below T_g) which only allowed the softened material (under the penetrating action of mold) flow in upward direction. Resultantly, an evident surface elevation on top of the PAZ took place (figure 3.5(a), figure 3.6 and figure 3.7). On the other hand, for $T_e=100^\circ\text{C}$, the softened substrate material flowed easily in all directions without yielding an elevated surface. As predicted also by the FE results, the cracks formed at the bottom edges of the channel during the UE process were shown in figure 3.5(b).

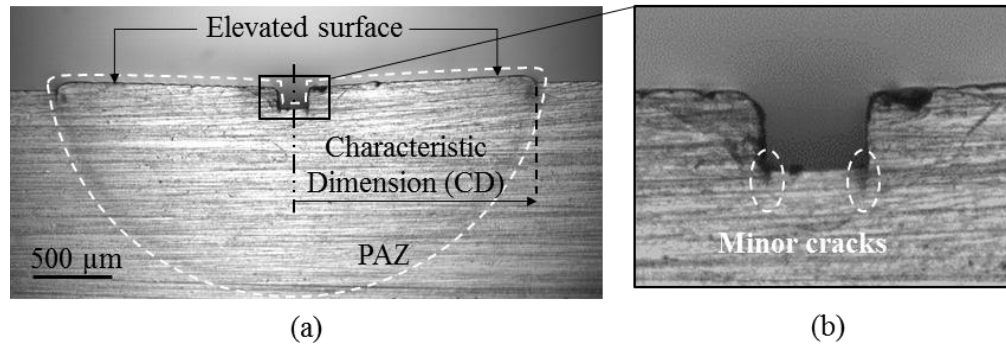


Figure 3.5 (a) Section view of the embossed channel (b) the minor cracks at the bottom edges of the channel.

As shown in figure 3.8, the best replication rates were 99.5% (r_w) and 100% (r_d) at $T_e=25^\circ\text{C}$ and $t_e=5$ s settings. When the substrate was preheated gradually up to 100°C , the r_d and r_w deviated from 100% resulting in incomplete channel geometries. At $T_e=100^\circ\text{C}$, 103% (r_w) and 93% (r_d) rates were obtained. However, preheating of the substrate above 80°C reduced the crack formations at the bottom edges of the embossed channels.

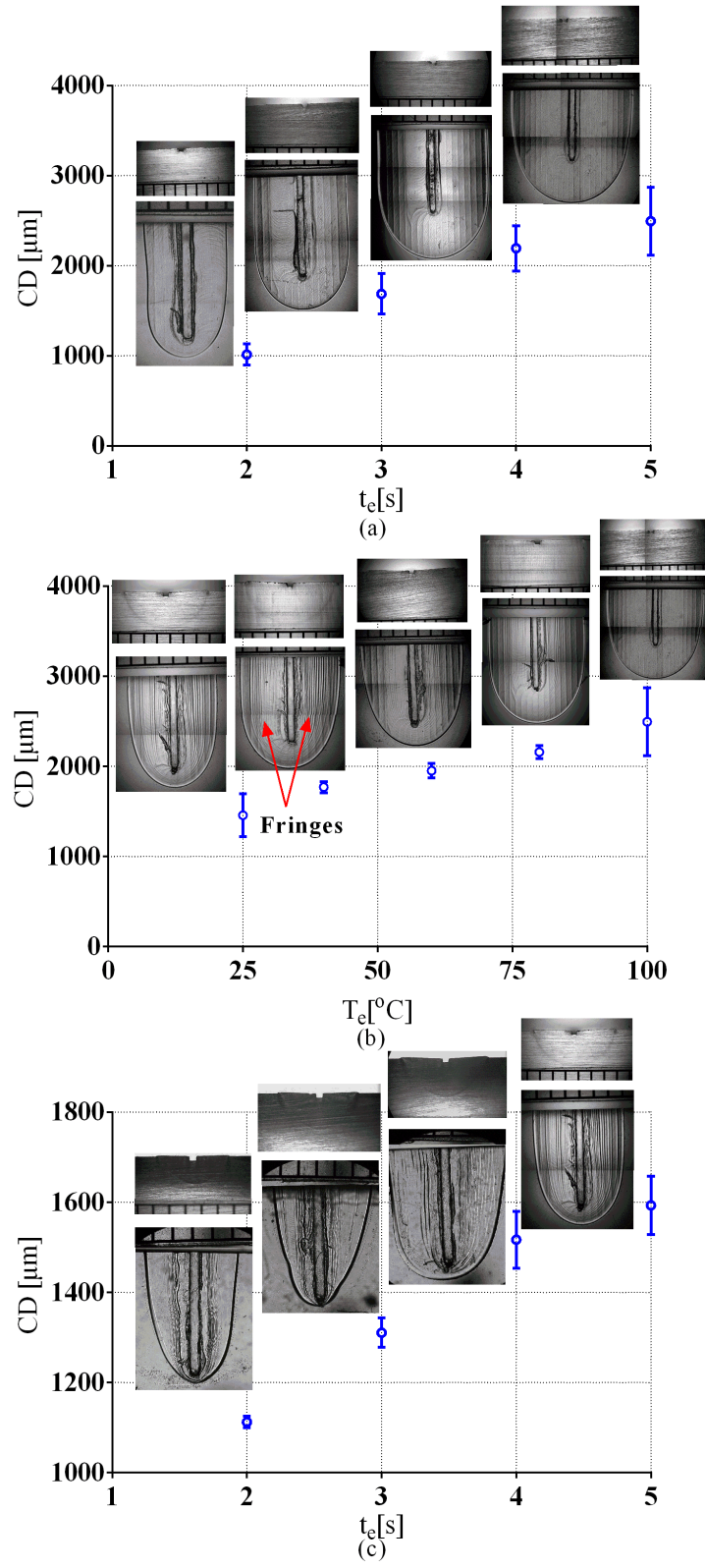


Figure 3.6 Average CD with (a) varying t_e settings at $T_e = 100^\circ\text{C}$, (b) varying T_e settings at 5 s, (c) varying t_e settings at $T_e = 25^\circ\text{C}$.

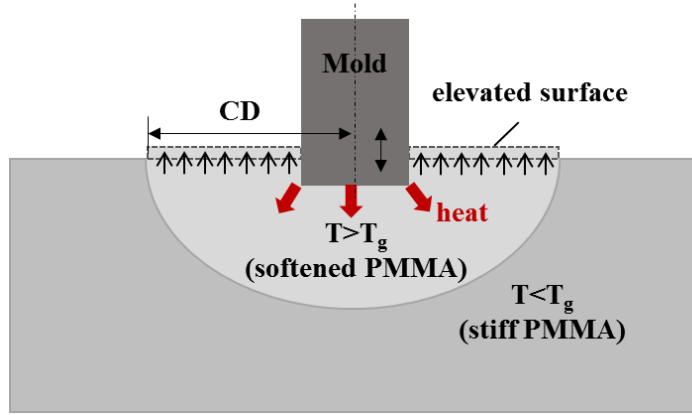


Figure 3.7 Representative view of PAZ.

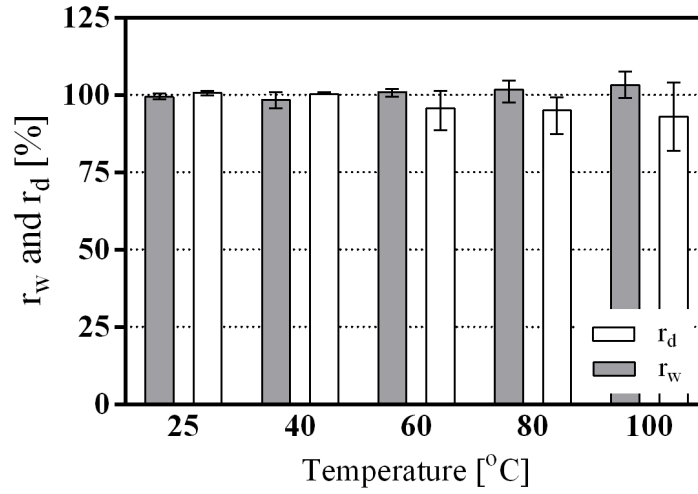


Figure 3.8 r_w and r_d for different embossing temperatures ($t_e=5$ s).

3.3.2 Load Measurement

Actual static force, F_{as} , and actual dynamic force, F_{ad} , transmitted to the PMMA during the UE process, were measured using a load cell and a strain indicator (figure 3.9(a)). The load cell was placed at the bottom of the brass holder (figure 3.9(b)). The mold (figure 3.9(d)), support plate (figure 3.9(e)) and PMMA substrate were placed on top of the load cell (figure 3.9(c)). The analog voltage output of the indicator was sent to computer by means of Arduino board for real time measurement of F_{ad} during

UE. In figure 3.10(a), the load cell calibration line is shown. The variation of the F_{ad} during UE process was given in Figure 3.10(b). The F_{ad} exceeds the static component F_{as} (85 N) in the first 0.5 s of the process. Then, F_{ad} reached to 100 N in 1 s and remained almost constant until the ultrasonic vibration was turned off. The higher value of F_{ad} than F_{as} was due to the hammering of vibrating sonotrode to the mold.

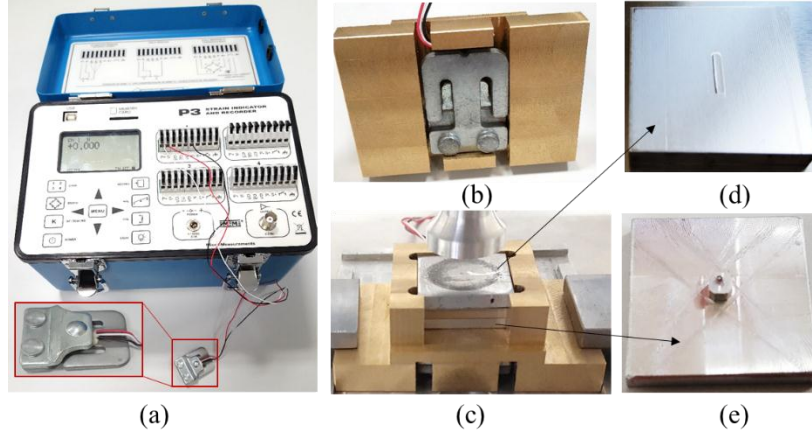


Figure 3.9 (a) Load cell mounted to strain indicator and recorder, (b) bottom view of load cell, (c) support plate, PMMA and mold arrangement, (d) mold, (e) support plate.

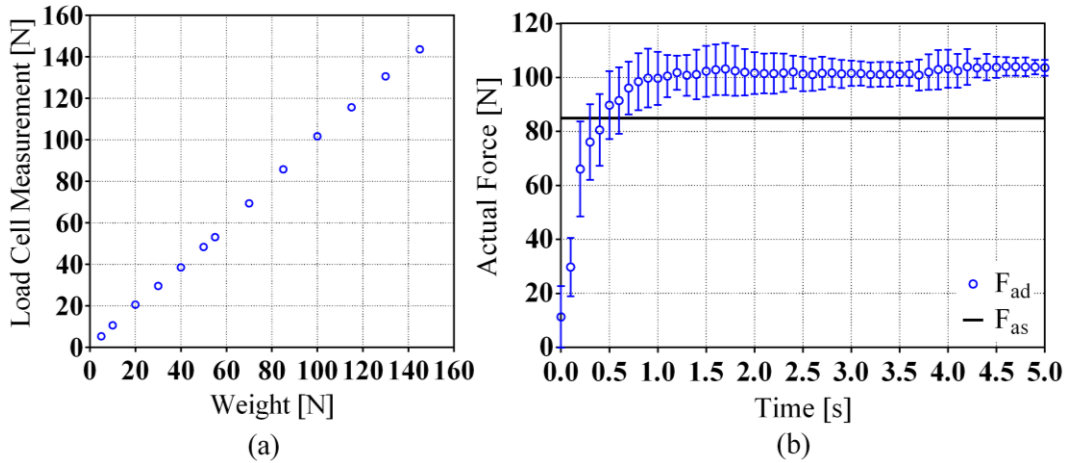


Figure 3.10 (a) Calibration line of the load cell, (b) variation of embossing force (F_{ad}) with embossing time for $t_e=5$ s, $T_e=25^\circ\text{C}$. Solid line indicates the static force applied by the dead weights.

3.3.3 Temperature Measurement of PAZ

During the process, a FLIR E5 thermal camera was used to monitor the average temperature (T_{av}) of PAZ and mold at the vicinity of the protrusion feature. One of the side walls of the brass holder was removed by milling to monitor the temperature clearly. The single protrusion mold pattern has been changed to the two protrusions (each 200 μm width, 150 μm depth and 3 mm length), which were located at the close vicinity of the mold side surfaces (figure 3.11). The PMMA emissivity (0.95), the reflected apparent temperature (28°C) and the distance to PMMA were set on the camera [87]. Temperature range of the camera was set to 100°C-145°C to filter the background signal. The temperature reading shown on the bottom left of the frame indicates the average temperature (T_{av}) of the region.

Near semi-circular shape of the PAZ and its change (i.e. CD values) with embossing time were in agreement with the numerical temperature distributions presented in figure 3.3(a). This resemblance implied the temperature increase beyond T_g within the PAZ during the UE process. So, the near semi-circular physical boundary of the PAZ was also bounded by an isothermal line at T_g . Since the temperature within the PAZ was above T_g , the substrate material was softened enabling plastic flow.

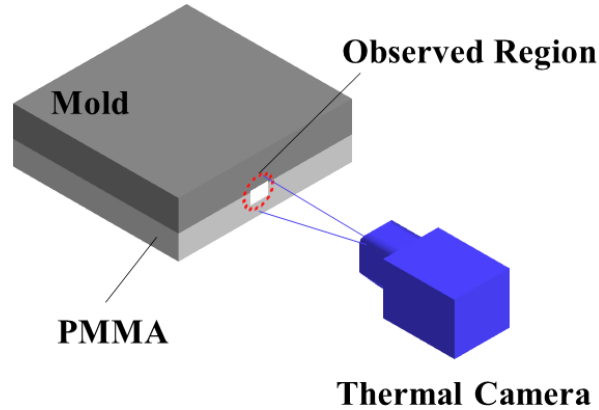


Figure 3.11 Schematic view of temperature measurement with thermal camera.

The temperature distributions obtained from FEM results (figure 3.3(a)) were added to figure 3.12 for easy comparison of numerical results and thermal camera readings. Thermal camera readings revealed the temperature increase at the vicinity of the mold protrusion right after the start of UE (figure 3.12(b)-(f)). The temperature exceeded T_g in the PAZ as predicted in the FEA. It is noteworthy that the temperature reached its maximum at $t = 5$ s. The isothermal lines at $t = 5$ s (figure 3.12(f)) was constructed by using OriginPro software package. Figure 3.12(h) verified the overlapping boundary of the PAZ with the isothermal line at T_g . Slight deviations observed were due to misorientation of the thermal camera with respect to the substrate and the mold. The discontinuities of the isothermal lines between the mold and substrate in the FEM analyses (figure 3.12(a)), which are not observed in the thermal camera results (figure 3.12(h)), are due to the lack of information about the thermal conductivity characteristics of the mold-PMMA interface.

In all experiments, a) the highest temperatures were observed at the contact regions between the mold pattern and PMMA, b) the T_{av} increased gradually till the end of the process, and T_{av} exceeded $T_g=107^\circ\text{C}$ at $t = 3$ s (figure 3.12(d)), c) the T_{av} increased from 84°C to 143°C at room temperature (for $T_e=25^\circ\text{C}$ experiments) (figure 3.13(a)) whereas it increased from 120°C to 134°C at $T_e=100^\circ\text{C}$ experiments with increasing t_e (figure 3.13(b)). T_{av} increased suddenly in figure 3.13(a) whereas the temperature increase was limited in figure 3.13(b) due to low strain energy emission (PMMA has low stiffness at 100°C).

The other observation worthwhile to mention concerning with the PAZ was the slightly opaque appearance of the substrate than the original. To find out the existence of the composition change in the PAZ, the original PMMA substrate samples was compared with the samples taken from the PAZ by means of Fourier Transform Infrared Spectroscopy (FTIR), thermogravimetric analysis (TGA) and differential thermal analysis (DTA). The results demonstrated well matching of the main material characteristics of the samples which revealed no change in structure of the PAZ material (figure 3.14(a)). TGA and DTA results verified no chemical composition change of the PMMA substrate after UE process (figure 3.14(b) and figure 3.14(c)). The opaque appearance of the PAZ was attributed to change in orientation of the

polymer chains under the severe UE process conditions (elevated temperature, ultrasonic vibration, hammering and frictional effects).

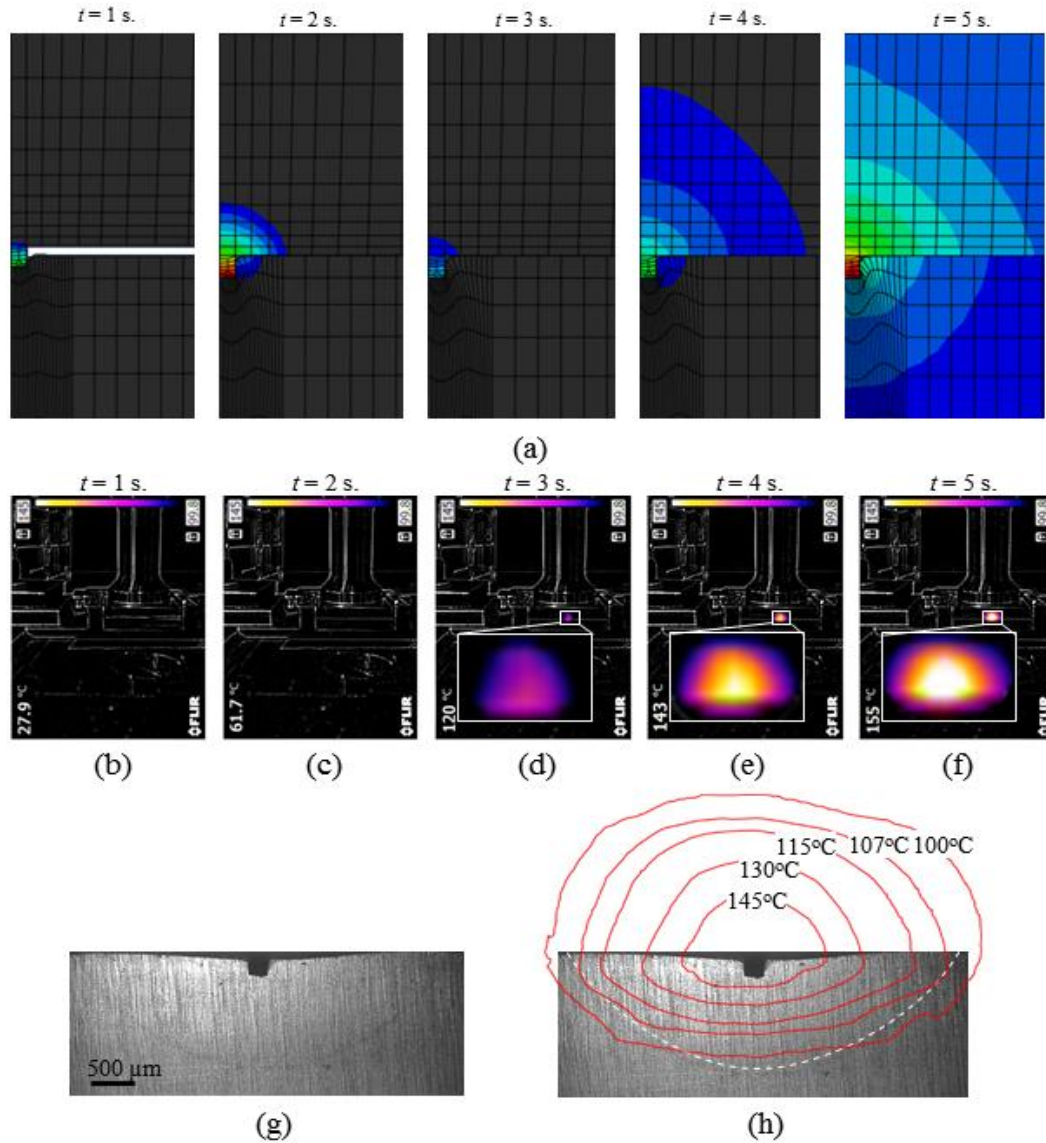


Figure 3.12 (a) Temperature distribution obtained from FEM. (b)-(f) Experimental temperature distribution across the mold and the substrate. (g) Section view of the experimentally embossed channel. (h) Isothermal lines overlaid with the section view of the channel.

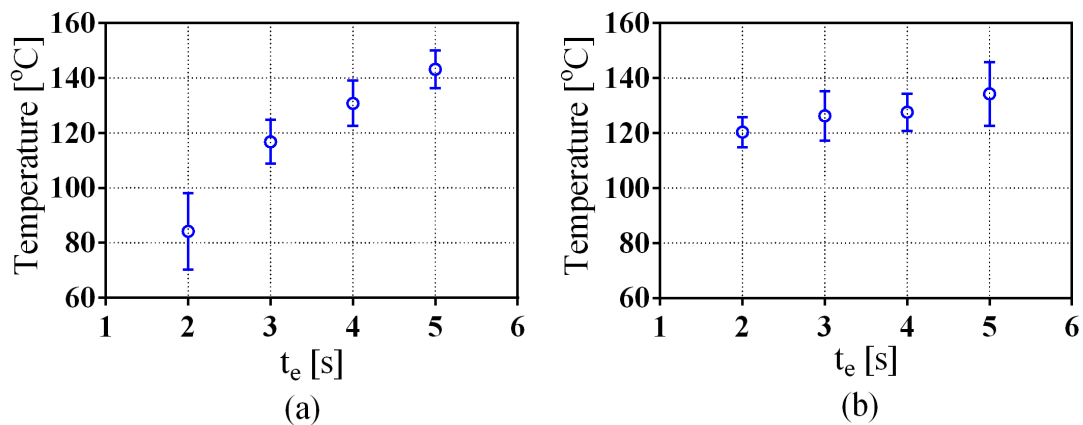


Figure 3.13 T_{av} with varying t_e for (a) $T_e=25^\circ\text{C}$, (b) $T_e=100^\circ\text{C}$. The bars indicate the standard deviations of the measurements.

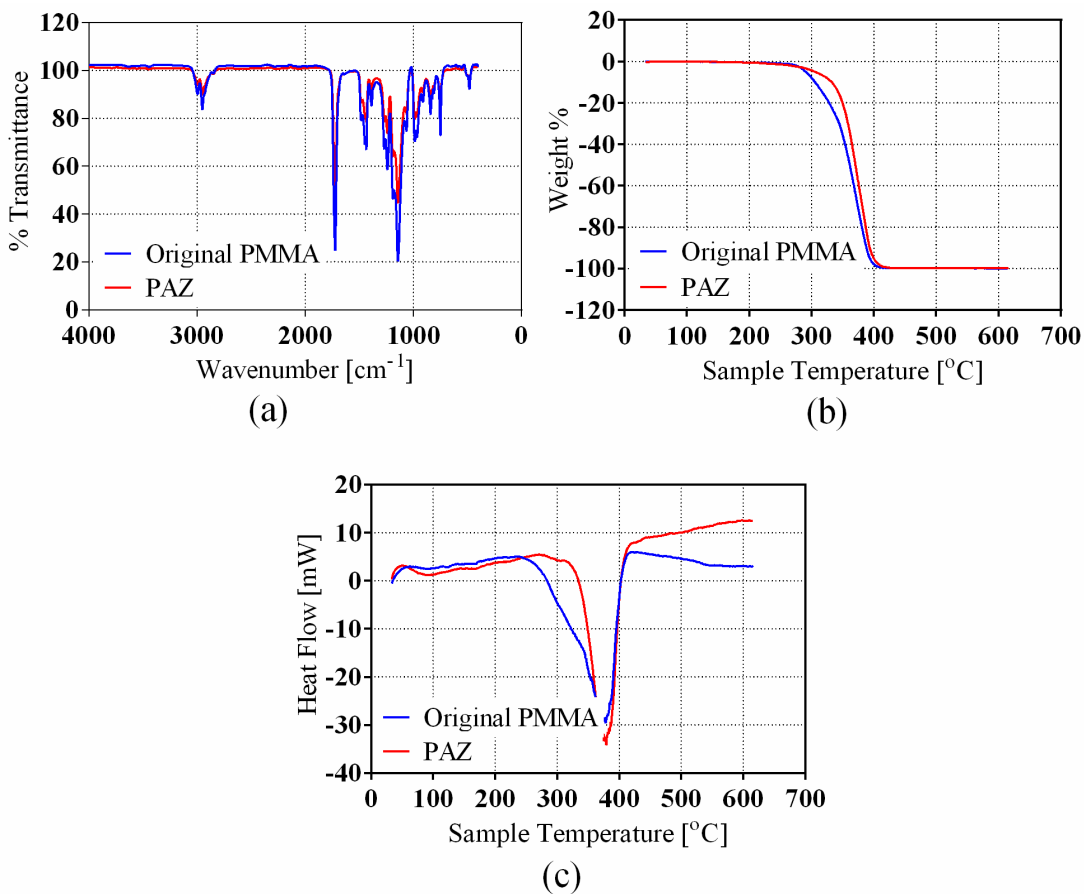


Figure 3.14 (a) FTIR analysis, (b) TGA and (c) DTA results.

3.3.4 Comparison of Experimental Work with FEM Results for PAZ

The numerical simulation and the experimental results regarding the deformation of the substrate during UE and PAZ formation were generally in good agreement (figure 3.15). A slight difference in temperature distribution was found between by the numerical model (figure 3.3) and the experiments (figure 3.12). In the numerical model, temperature increased until $t = 2$ s. The mold and the substrate cooled down starting at $t = 2$ s and end at $t = 3$ s since the hammering affect ceased at $t = 2$ s. After $t = 3$ s, both the mold and the substrate heated up again due to friction between the mold and the substrate till the end of the process and reached its maximum at $t = 5$ s. The numerical and experimental results revealed that maximum temperature occurred at $t = 5$ s. However, the monotonically increase in temperature during the process was not predicted well by the numerical model. The deviation in the numerical model and the experimental results was attributed to the lack of information regarding the actual stress-strain data and viscoelastic material behavior of PMMA at high strain rates and temperatures.

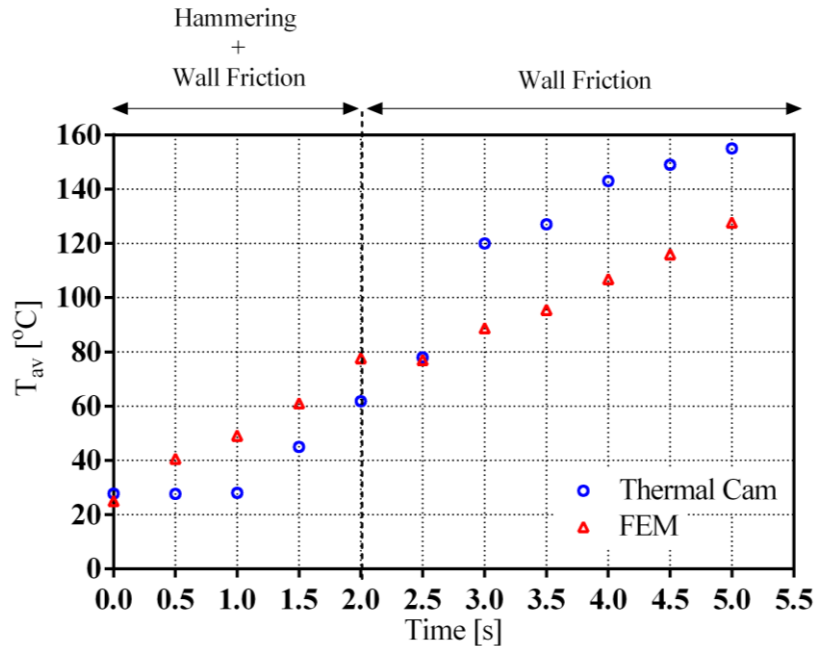


Figure 3.15 Comparison of T_{av} for FEM and temperature results of thermal camera ($t_e=5$ s, $T_e=25^\circ\text{C}$).

3.4 Discussion and Conclusion

In this work, we presented an in-depth investigation to understand the mechanism of ultrasonic embossing process for fabrication of thermoplastic microfluidic chips. Firstly, we developed a numerical model to describe how the substrate deforms under combined ultrasonic vibration and static load, and determine the temperature distribution across the mold and the substrate during the process. Then we carried out experiments to verify numerical findings.

In this study, 200 μm wide and 150 μm high straight channels were successfully embossed on 3 mm thick PMMA substrates at 85 N static load, 28 kHz vibration frequency at 10 μm amplitude. The channels were penetrated in 2 s at room temperature. According to the numerical modelling of the UE process, in this period, hammering action of the vibrating mold and the friction between the mold and the channel wall were effective. Right after this period, the wall friction was responsible for the channel replication. The continuation of the process beyond the end of hammering improved the replication rates (99.5% and 100% for the width and the depth replication rates).

A semi-circular region around the channel cross-section which was defined as the process-affected zone (PAZ) was common in the experiments. It is observed numerically and experimentally that the PAZ was bounded by the isothermal surface at the T_g of the substrate. The investigations on composition of the substrate within and out of the PAZ showed that the material composition remained unchanged during the process.

Numerical model revealed equivalent stresses exceeding the ultimate strength of the substrate material (less than 70 MPa at above 25°C for PMMA) at the bottom edges of embossed channel during the process. These stresses caused minor crack formations after UE experiments. Experimental results showed that preheating considerably reduced the cracks since the overall substrate was softened. However, preheating resulted in undesired deformation of overall substrate as well as poor replication rates. So, the preheating should not be considered unless the cracks are

needed to be strictly avoided. On the other hand, we believe that the minor cracks could be cured after the process by a suitable solvent vapor treatment [88].

Results of the numerical simulation and the experiments generally agree well in explaining the deformation of the substrate during UE and PAZ formation. However, it was observed that the temperature monotonically increased during the process, which is not predicted by the numerical model. The difference between the numerical model and the experimental results is basically attributed to unavailability of actual stress-strain data, viscoelastic material behavior for PMMA at high strain rates and process temperatures and heat conduction characteristics of mold-PMMA interface. This indicated the need for material testing at high strain rates and process temperatures for the materials used in UE.

The rare occurrence of improper surface roughness as well as geometrical deterioration of embossed channels due to excessive local heating in a fraction of a second can be reduced by closely controlling the vibration amplitude, frequency, force and time settings.

The experimental studies also revealed the importance of substrate thickness in the embossed channel quality. The variation in the thickness results in local temperature fluctuations causing incomplete channel formations.

CHAPTER 4

FABRICATION OF A DROPLET GENERATOR CHIP BY UE

The use of silicon and glass materials in microfluidic devices fabrication which started with semiconductor industry requires clean-room microfabrication methods [89, 90].

The commercialization of microfluidic devices forces low cost fabrication of medium to high volume production instead of expensive clean-room fabrication methods [91]. Development of polymer based microfluidic fabrication methods enable manufacture of polymer based (elastomers and thermoplastics) devices with low cost, biocompatibility, transparency and large production volume [89]. Among the other thermoplastic materials, PMMA is the commonly used one for disposable microfluidic chip production due to its low cost, excellent optical transparency, high strength characteristics and production convenience [92, 93].

LOC devices based on droplet-based microfluidics enable easy formation and close control of highly monodisperse droplets [94-96]. The droplet-based microfluidics are highly promising for biomedical research and applications such as encapsulation of biological substances and forming spheroids as scaffold [97-102]. The hydrogel droplets are used as templates to encapsulate cells inside to function as tissue building blocks (bioprinting) [103].

In the scope of the thesis, the droplet based microfluidic chip was produced by UE technique whereas mold was formed by milling process. The applicability of the UE chip in droplet formation was one of the important metric of the chip performance. To the best of knowledge of the author of the thesis, there is no published work on the droplet formation by using a chip produced by UE technique as well as using a mold manufactured by milling process for replication of the micro channels. This chapter summarizes the efforts put forward at this respect. At the initial phase of the study, the droplet formation was numerically simulated and validated afterwards with experiments for Si oil (continuous phase) and water (dispersed phase). Then, the

dispersed phase was replaced with a hydrogel solution to form hydrogel droplets. Moreover, the initial efforts spent to cure the formed droplets under ultra violet (UV) light exposure were presented.

4.1 Droplet Generator

The droplet based systems are affected by several dimensionless numbers. These are; the ratio of inlet liquid flow rates, ratio of viscosities, ratio of geometrics and capillary number (Ca). Among these, the most effective parameter which dominates the droplet formation is Ca . Ca is defined as the ratio (generally between 10^{-3} and 10 [104]) of the viscous forces to interfacial forces.

$$Ca = \frac{\mu \vartheta}{\sigma} \quad (4.1)$$

where μ is dynamic viscosity, ϑ is flow velocity and σ is the interfacial tension. For $Ca < 1$, the flow dominates by σ and spherical droplet formations occur in the channel. For $Ca > 1$, the flow dominates by viscous forces which results in the asymmetric droplet formations [105].

T-junction and flow focusing geometries were generally used in the droplet based microfluidic devices. In T-junction geometry, the two phases flowing in the channel confront in the junction resulting in formation of droplets (figure 4.1(a)). In flow focusing geometry, the continuous phase flowing in two opposite channels squeezes the dispersed phase flow in the middle channel (figure 4.1(b)). Then, the dispersed and the continuous phase flow together through the orifice. At the end, the dispersed phase flow gets narrower and forms monodisperse droplets [105].

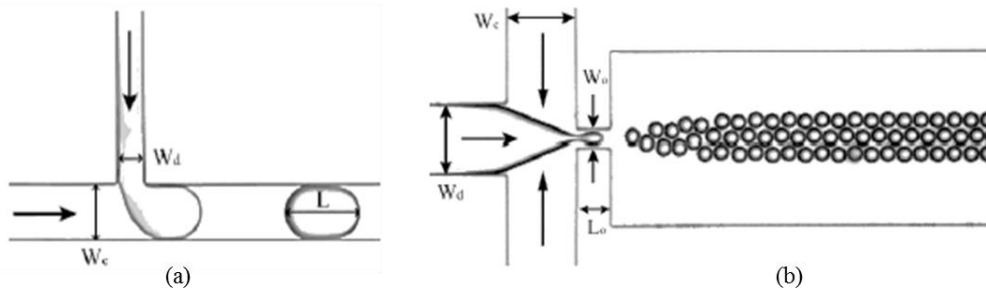


Figure 4.1 Droplet generation in (a) T-junction geometry, (b) flow focusing geometry [105].

4.1.1 Modeling of Droplet Generator

In this study, the flow focusing geometry was used for the droplet formations. At first, the flow rates of the dispersed and continuous phases to form the monodisperse droplets were found by using the hydraulic resistances of the channels. The hydraulic resistance of each channel can be expressed using the Ohm Law analogy for electric resistor (figure 4.2(b)). In a channel, the pressure drop, ΔP can be calculated as:

$$\Delta P = RQ \quad (4.2)$$

where R is the hydraulic resistance of the channel and Q is the flow rate of the liquid.

The hydraulic resistance of a channel is related with length, width and height of the channel as well as the viscosity of the liquid flowing in the channel. For rectangular and circular channels, the hydraulic resistances are calculated as:

$$R_{rect_channel} = \frac{12\mu L}{wh^3 \left[1 - \frac{h}{w} \left(\frac{192}{\pi^5} \sum_{n=1}^{\infty} \frac{1}{(2n-1)^5} \tanh\left(\frac{(2n-1)\pi w}{2h}\right) \right) \right]} \quad (4.3)$$

$$R_{circ_channel} = \frac{8\mu L}{\pi r^4} \quad (4.4)$$

where L , w , h , r are the length, width, height and radius of the channel, respectively, and μ is the dynamic viscosity of liquid.

After the junction, the viscosities of the two phases together should be taken into account in calculation of hydraulic resistance since water droplets are formed in the Si oil. The droplet formation causes higher pressure drop (ΔP) along the channel. ΔP can be calculated by summing up the pressure drop for Si oil (ΔP_i) and for n number of water droplets along the channel ($n\Delta P_d$) (eqn. (4.5)).

$$\Delta P = \Delta P_i + n\Delta P_d \quad (4.5)$$

So, the channel resistance after the junction can be described as:

$$R_{droplet_channel} = R_{oil}(1-\phi) + n(3.15 \frac{2\sigma}{h} Ca^{2/3} \frac{1}{9wh}) \quad (4.6)$$

where R_{oil} is the resistance of the channel for oil flow only, ϕ is the volumetric ratio of water in the channel, σ is the surface tension, Ca is capillary number and g is the droplet flow velocity.

In the simulation studies, 10 cSt Si oil (9.3 mPa.s dynamic viscosity, 930 kg/m³ density) was used as continuous phase and distilled water (DW) was used as dispersed phase. Vacuum pressure was applied to the output of the channel by using vacuum pump (figure 4.2(a)) in order to control the flow rates of the two phases. A prepared Matlab code was used to calculate the hydraulic resistance of the channels and flow rates of Si oil and DW water. Different channel dimensions and vacuum pressure values were tried by using the code. A 10 kPa vacuum pressure was found as a suitable level to be used throughout the study. The resistances of the channel with droplets were calculated by using eqn. (4.3) and eqn. (4.6) separately. Then, the flow rates were found by using these values. Since the difference between the two flow rates was low (0.74 μ l/min or 0.09%), eqn. (4.3) was used for the calculation of the resistances throughout the study.

The hydraulic resistances of the channels and flow rates of the phases (figure 4.3) were calculated for the nominal channel dimensions given in Table 4.1. Since, the actual channel dimensions were slightly different than the nominal values due to mold milling inaccuracies, the values were recalculated after production of the mold.

“Phase field method” was used in the analysis for obtaining the interfacial motion of the multiphase flow. The multiphase flow is defined with ϕ ($\phi = 1$ for dispersed phase, $\phi = 0$ for continuous phase, through the interface $0 < \phi < 1$). Time dependent Navier Stokes (eqn. (4.7)) and total energy (eqn. (4.8)) relations were solved simultaneously for the flow in concern. An incompressible flow ($\nabla \cdot \mathbf{u} = 0$) was assumed in the analysis.

$$\rho \frac{\partial \mathbf{u}}{\partial t} + \rho \mathbf{u} \cdot \nabla \mathbf{u} = -\nabla p + \nabla \cdot \mu (\nabla \mathbf{u} + (\nabla \mathbf{u})^T) + \mathbf{F}_{st} \quad (4.7)$$

$$\frac{\partial \phi}{\partial t} + \mathbf{u} \cdot \nabla \phi = \nabla \cdot \frac{\kappa \lambda}{\varepsilon^2} \nabla \psi \quad (4.8)$$

$$\psi = -\nabla \cdot \varepsilon^2 \nabla \phi + (\phi^2 - 1)\phi \quad (4.9)$$

In the equations (4.7)-(4.9), u , p , t , ρ , μ , F_{st} , κ , λ , ε are the velocity (m/s), pressure (Pa), time (s), density of flow (kg/m³), viscosity of flow (Pa.s), force due to the surface tension (N), mobility (m³.s/kg), mixing energy density (N) and interface thickness (m), respectively. The ρ and μ were calculated by using the ϕ value (eqn. (4.10) and eqn. (4.11)). The indices in the equations describe the two different phases.

$$\rho = \rho_1 + (\rho_2 - \rho_1)\phi \quad (4.10)$$

$$\mu = \mu_1 + (\mu_2 - \mu_1)\phi \quad (4.11)$$

ε is increased with increasing κ depend on the diffusion between the phases. This relation can be expressed as:

$$\gamma = \chi \varepsilon^2 \quad (4.12)$$

where χ is the mobility control parameter. In this study, ε was defined as the half of the largest element size. In order to find λ , the following relation was used in the analysis:

$$\sigma = (2\sqrt{2}\lambda) / (3\varepsilon) \quad (4.13)$$

In order to get reliable results in numerical analysis of the above mentioned flow focusing geometry, the resolution of meshing must be very high causing extremely high number of elements in 3D modelling. The 3D modelling will result in extremely long computation time. Due to this reason, 2D modelling of the flow focusing geometry was preferred in this study. 2D flow modelling brings the assumption of no flow variation in depth direction which is valid only for high height to width channel ratio. In order to solve this problem, “shallow channel” approach was used in the 2D model. This approach disregards the pressure variation in parallel axis of the channel height for very low channel height to hydraulic diameter ratio ($h/D \ll 1$). In this

approach, the flow is assumed to take place in a parallel plane to the channel bottom. The solution is provided by adding a force term (given below) to eqn. (4.7).

$$F_{\mu} = -\frac{12\mu u}{h^2} \quad (4.14)$$

The calculated flow rates and channel dimensions were input to COMSOL Multiphysics 5.3a software package to observe if monodispersed droplets were formed for the flow focusing geometry. If monodispersed droplets were not formed, then channel dimensions and flow rates were revised. In this study, flow rates given in figure 4.3 were input to the software. The simulations were conducted for 0.1 s. The convergence tests showed the convenience of 30000 element meshing (no significant variation beyond this level) in the simulations.

The stages of droplet formations were presented in figure 4.4. The droplet formation frequency was found as 70 Hz (droplet/s). The droplet diameter and the center distance between two successive droplets were found as 135 μm and 390 μm , respectively by using ImageJ software package.

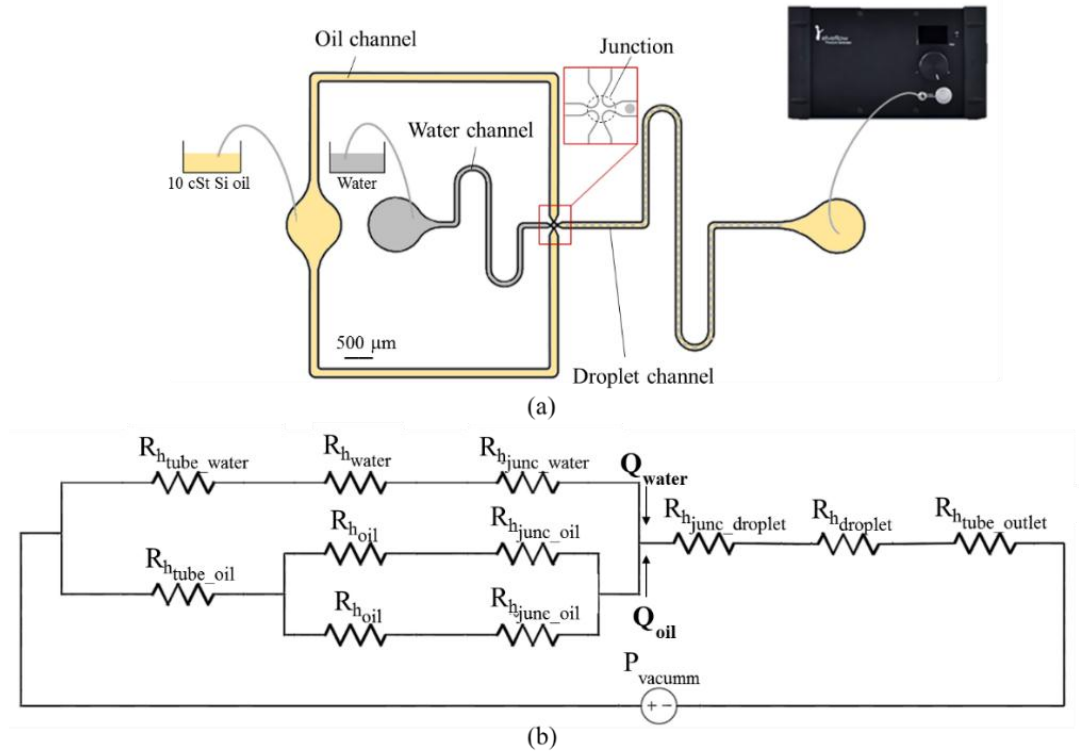


Figure 4.2 Schematic view of designed chip, (b) Modelling of the chip with electrical circuit analogy.

Table 4.1 Dimensions of the channels.

	Length [μm]	Nominal width [μm]	Actual width [μm]	Nominal depth [μm]	Actual depth [μm]
Dispersed phase (water) channel	12200	160	120		
Continuous phase (Si oil) channel	18640	300	300	40	32
Droplet channel (after junction)	25900	200	165		
Junction channels	100	50	50		

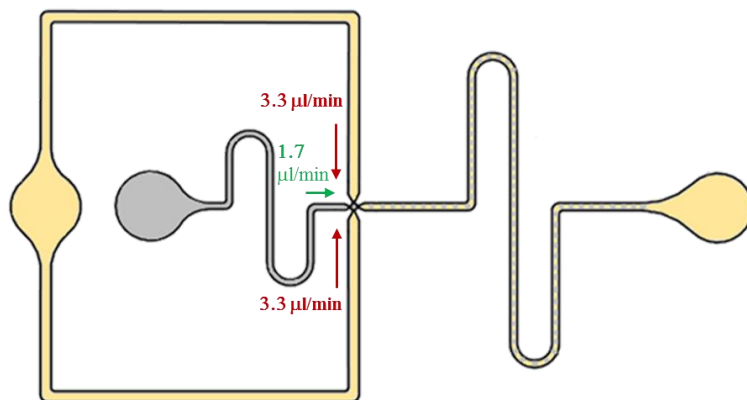


Figure 4.3 Flow rates of the inlet channels.

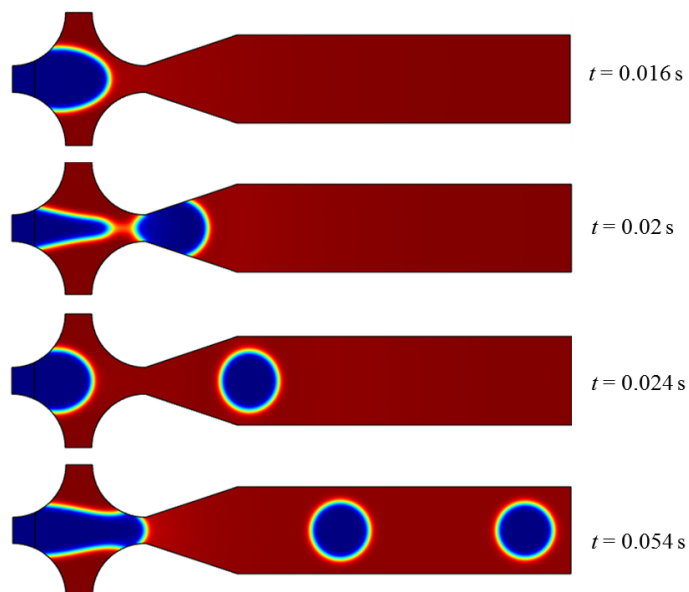


Figure 4.4 The droplet formations at various times.

4.1.2 Fabrication of the Chip

After having successful monodispersed droplets formations, the channel dimensions found by using numerical analysis were used in fabrication of a droplet generator.

The mold pattern used to replicate the flow focusing geometry (figure 4.5(a)) was designed by Solidworks package. The G-code (part program) was generated by

Solidcam software. A 40 μm nominal height pattern was micromilled on 23x23x3 mm aluminum AA7075 material using 1 mm (3500 rpm and 100 mm/min) and 0.2 mm micromilling cutters (3500 rpm and 5 mm/min) with ProLight WPLM1000 machining center (figure 4.5(b)). The milling performed was in accordance with the procedure described in Chapter 2, section 2.3. The total production time for milling was 1 hour.

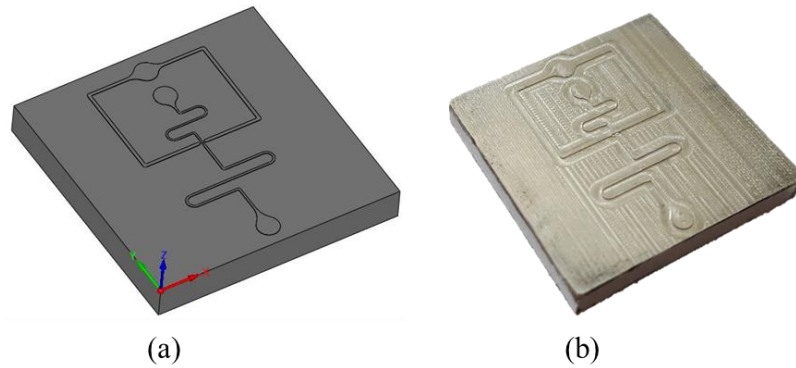


Figure 4.5 (a) The mold pattern design, (b) micromilled mold pattern.

Since the best replication rates were obtained at room temperature (as mentioned in Chapter 3), the chip embossing process on 23 x 23 x 3 mm PMMA substrate by UE was conducted at $T_e=25^\circ\text{C}$. The best channel geometrical details and replication rates were obtained at 15 s embossing time and 85 N force. The substrates with replicated channels were sealed with 75 x 25 x 3 mm blank PMMA. The replicated substrate and the blank PMMA were exposed to chloroform vapor for 1.5 min. The blank PMMA and the replicated substrate were sealed with thermo-compressive bonding at 80°C for 4 min under 5 kN force. So, the mold milling, UE and sealing time for a chip took about totally 1 hr 6 min. Since the mold milling time was spent once even for large number of chips, the production time for a chip was less, such as 12 mins/chip for a party of 10 chips whereas 6.6 mins/chip for a party of 100 chips. For thinner substrates, the compressive bonding time could be reduced down to some ten seconds. A bonded PMMA chip was shown in Figure 4.6.

The sealing of the replicated substrate couldn't be achieved by ultrasonic welding equipment available, since power of the ultrasonic source (500 W) is low for the chip bonding area and thickness of the replicated substrate (3 mm) in use.

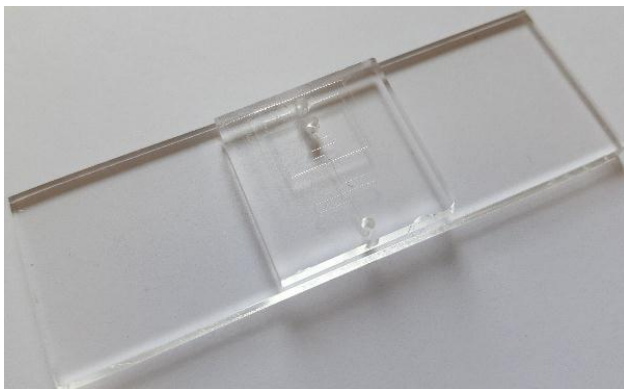


Figure 4.6 UE chip sealed with solvent assisted thermo-compressive bonding.

4.1.3 Chip Characterization

The PMMA chip (figure 4.6) was tested by introducing 10 cSt Si oil and DW to the inlets (with PTFE (polytetrafluoroethylene) tubes) and applying 10 kPa vacuum pressure (applied with ELVEFLOW vacuum pump) to the chip outlet. The DW droplet formations were recorded with high speed camera of the Lily MCX500 type microscope. The droplet flows were recorded at 170 frame/s (figure 4.7(a)). The formation stages of a droplet at the junction were shown in figure 4.7(b).

In this study, a digital video processing program, Droplet Morphometry and Velocimetry (DMV) [106], was used for the characterization of droplet diameters, the droplet formation frequency and the distances between the droplets recorded at 170 frame/s rate.

The average droplet size and the average distance between the droplets were found as 157 μm (figure 4.8(a)) and 439 μm (figure 4.8(b)), respectively. The low coefficient of variance (CV) of the droplet diameter (0.6%) and the distance between droplets distributions (1.1%) indicated the highly acceptable shape uniformity and

formation repeatability of droplets. The droplet formation frequency was 61 Hz. The slight deviations of COMSOL simulation results from experimental findings (14% for droplet diameters and 11% for the distance between droplets) were attributed to imperfections on the channel surfaces, variations in cross-sections along the channel (due to deflection of micromilling cutter in mold pattern machining) and deviations of actual viscosity of Si oil and DW from the theoretical values used in the COMSOL analysis.

After proving acceptable performance of the UE chip in droplet formation by using Si oil and DW phases, the hydrogel droplet formation for bioprinting was tested. In bioprinting applications, naturally derived biocompatible hydrogels or synthetic ones such as collagen, alginate, gelatin, polyethylene glycol (PEG) and polyacrylic acid (PAA) based hydrogels were used [107, 108]. In our study, PEG hydrogel solution and 10 cSt Si oil were used as dispersed phase and continuous phase, respectively. The dispersed phase solution consisted of 10% polyethylene glycol diacrylate (PEG-DA) solution in water (dynamic viscosity 57 mPa.s, density 1120 kg/m³).

After formation of hydrogel droplets, the curing process (typically performed with ultra violet (UV) light) was required to prevent merging of droplets and preservation of biological substances in the droplets. In this study, the PEG-DA hydrogel droplets were cured with UV light. For rapid curing of the hydrogel droplets, first, the Irgacure 2959 photo initiator was dissolved in n-vinyl pyrrolidinone (NVP) accelerator (at 100 mg/ml proportion) [109] and 60 µl of this solution is added to 3000 µl PEG-DA solution.

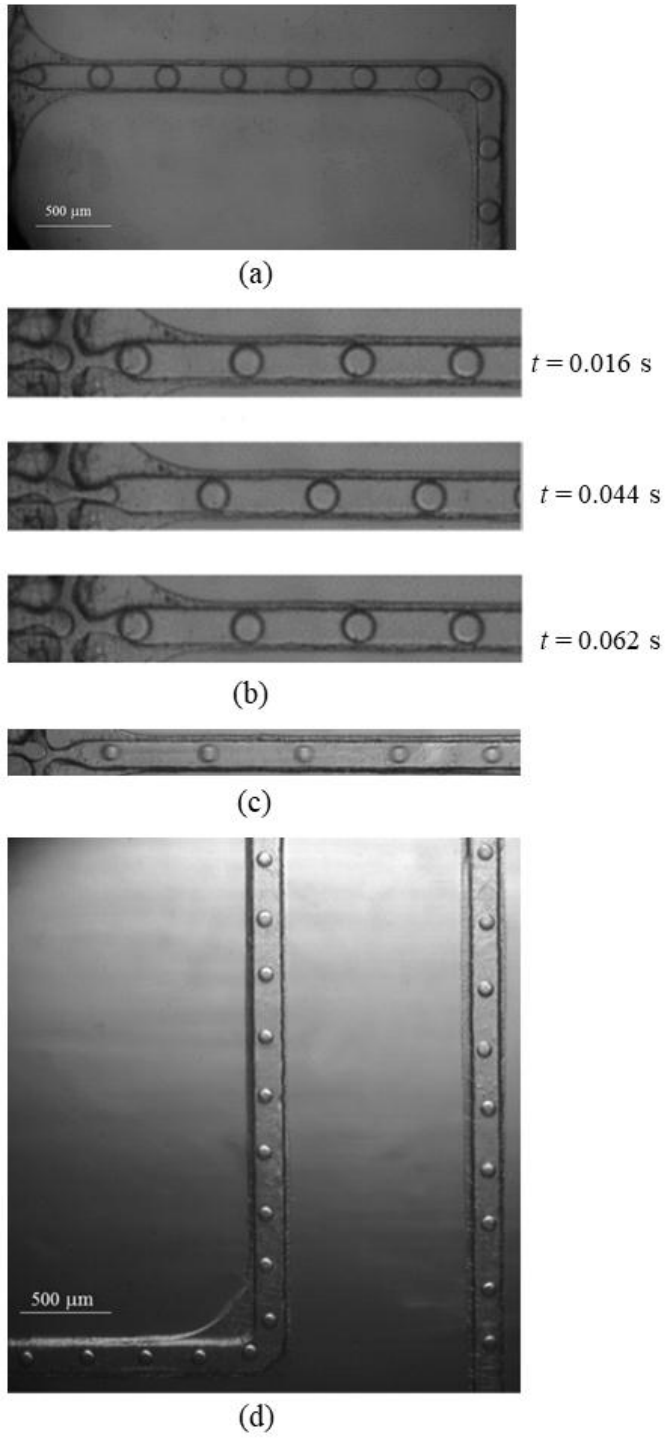


Figure 4.7 (a) DW droplets formed after junction, (b) stages of formation of DW droplets at the junction, (c) hydrogel droplets formed after junction, (d) arrangement of hydrogel droplets in the channel.

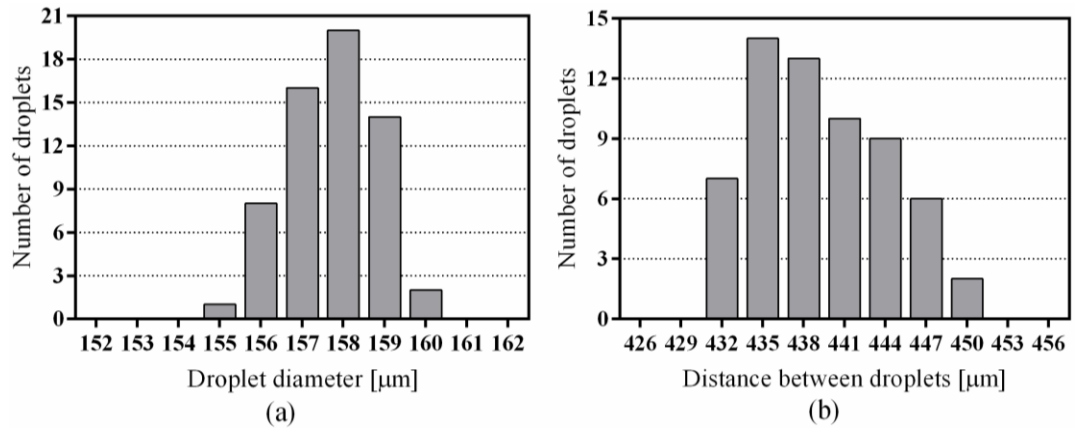


Figure 4.8 Distributions of (a) droplet size and (b) the average distance between the droplets (sample size=61).

The hydrogel droplets formed at 10 kPa outlet port vacuum pressure were shown in figure 4.7(c) and figure 4.7(d). The average diameter of hydrogel droplets and average distance between the gel droplets were found as 85 μm and 350 μm, respectively. The shape uniformity and formation repeatability of droplets were acceptable. The PTFE tube connections to the inlets and outlets of the chip were covered with aluminum foil and the chip surface before the junction was covered by black vinyl tape to prevent the UV light exposure. Then, the chip was placed under 36 W UV light (365 nm peak wavelength, 30 mW/cm² light intensity). No curing of droplets was observed during the process since each droplet emerged out of the chip less than a second. Then, the travel of the droplets in the droplet channel was stopped by ceasing the vacuum pressure and the UV light was applied to the chip. A 1 min UV light exposure was found sufficient for curing the droplets. The cured droplets were appeared in opaque colour.

4.2 Discussion and Conclusion

In this part of the study, the UE chip produced by means of a mold, machined with a CNC micro milling, was used successfully for forming monodispersed distilled water as well as PEG-DA hydrogel droplets. The hydrogel droplets formed were also cured inside the chip by using UV light exposure at about 30 mW/cm² light intensity. The COMSOL numerical simulation results and experimental findings for droplet size

and frequency as well as distances between the droplets were consistent. Moreover, overall production timing of a chip for a large volume was short considering the other LOC production techniques. The UE chip fabrication trial in this study could be considered as a pioneer work since it proved the suitability of the UE technique for production of a LOC without using expensive and time consuming clean room fabrication techniques. The preliminary droplet curing studies indicated the need for further efforts on optimization of PEG-DA composition and UV light intensity for minimizing exposure time.

CHAPTER 5

CONCLUDING REMARKS AND FUTURE WORK

In this work, in-depth experimental and numerical investigations to understand the mechanisms of hot embossing (HE) and ultrasonic embossing (UE) processes were conducted for fabrication of thermoplastic microfluidic chips.

In HE, microchannel replication rates on PMMA substrates for varying embossing temperature, force, and time were investigated experimentally for different micromilled aluminum mold protrusion widths (56-436 μm). The increasing temperature up to 115°C enhanced the replication rate (the best value is 130% in width for 56 μm width channel) since it improved filling of the protrusion root cavities, thus eliminating the swallowtail defects. Above this temperature, excessive lateral deformation and thinning of the substrate was observed. For all experimental settings even at the lowest temperature setting of 100°C, embossing wider channels than 200 μm yielded perfect replications. Statistical analysis (ANOVA) of experimental results revealed the importance of temperature on width replication rates whereas impact of force and time were relatively low. Substrate material flow behavior during embossing, especially at low temperature settings, caused skewness of the replicated channels. The FEA findings were consistent with the experimentally observed skewness formations depending on mold protrusions locations and density.

In the second stage of the study, a numerical model for UE was developed to determine substrate deformations under combined ultrasonic vibration and static load, as well as the temperature distribution across the mold and the substrate during the process. Then experiments were carried out to verify the numerical findings. 200 μm wide and 150 μm high straight channels were embossed successfully on 3 mm thick PMMA substrates in 2 s at room temperature by applying 85 N static load and an ultrasonic vibration at 28 kHz, with an amplitude of 10 μm . The numerical model revealed the effectiveness of hammering action of the vibrating mold plus the friction between the mold and the channel wall in the first 2 s of UE process. After the first 2

s (up to 5 s), the wall friction was responsible for the channel formation and this time period was necessary for better replication rates (99.5% width and 100% depth replications are reached at $t_e=5$ s). An ellipsoidal region was observed around the channel cross-section during the experiments, which was defined as the process-affected zone (PAZ). Numerical and experimental analyses revealed the existence of isothermal surface at T_g of substrate (107°C for PMMA) binding the PAZ. Therefore, only the material within the PAZ softened, leaving the rest of the material stiff. The interface between the stiff material and the softened material defines the typical semi-circular PAZ boundary. The FTIR and TGA test results indicating unchanged material composition in the PAZ during the UE process, was valuable since material composition is important in microfluidic applications where biocompatibility is essential. Numerical model of UE showed that equivalent stress exceeds the ultimate strength of the substrate material at the bottom edges of embossed channel during the process. In accordance with this numerical result, minor cracks at the bottom edges of the channel were also observed experimentally. The preheating of the substrates to 100°C, which was very close to T_g of PMMA, considerably reduced the cracks since the overall substrate was softened. However, preheating resulted in undesired deformation of substrate and lower replication rates.

The numerical simulation and the experimental findings generally agreed well in explaining the deformation of the substrate and PAZ formation during UE. The temperature increase monotonically during the UE process could not be predicted well by the numerical model due to unavailability of actual stress-strain data and viscoelastic material behavior for PMMA at high strain rates and process temperatures. For HE and UE replicated channels, the successful bonding results were obtained by solvent assisted thermo-compressive bonding technique.

The micromilling process in machining molds (patterns down to 50 μm width and 32 μm depth) was used successfully in UE replication of LOC channels. The performance of hydrogel droplet generator chip fabricated by using the UE technique and micromilled molds proved the suitability of the technique for production of LOC devices.

The studies conducted in UE revealed the need for further efforts in the following issues to reach a higher level of completion in the field; a) polymer substrate material testing at high strain rates and process temperatures used in UE, b) ultrasonic bonding of microfluidic chips, c) bioprinting applications by using UE replicated chips.

REFERENCES

- [1] V. Scognamiglio, G. Rea, F. Arduini and G. Palleschi (Eds.). *Biosensors for sustainable food: new opportunities and technical challenges*. Cambridge, MA: Elsevier, 1st ed., vol 74, 2016, p. 450.
- [2] Z. Zhou, Z. Wang and L. Lin (Eds.). *Microsystem and nanotechnology*. Springer-Verlag, Berlin, 2012, p. 1004.
- [3] Y. Xia and G. M. Whitesides, “Soft lithography,” *Annu. Rev. Mater. Sci.* vol. 28, pp. 153–84, 1998.
- [4] D. C. Duffy, J. C. McDonald, O. J. A. Schueller, and G. M. Whitesides, “Rapid prototyping of microfluidic systems in poly(dimethylsiloxane),” *Anal. Chem.*, vol. 70, no. 23, pp. 4974–84, 1998.
- [5] V. Silverio and S. C. de Freitas. *Microfabrication Techniques for Microfluidic devices*. In Francisco José Galindo-Rosales (Eds.), *Complex Fluid-Flows in Microfluidics*, Springer, 2018, pp. 25-51.
- [6] X.-M. Zhao, Y. Xia and G. M. Whitesides “Soft lithographic methods for nanofabrication,” *J. Mater. Chem.*, vol 7, no. 7, 1069–74, 1997.
- [7] G. M. Whitesides, E. Ostuni, S. Takayama, X. Jiang and D. E. Ingber, “Soft lithography in biology and biochemistry,” *Annu. Rev. Biomed. Eng.*, vol. 3, no. 1, pp. 335–73, 2001.
- [8] J. C. McDonald, D. C. Duffy, J. R. Anderson, D. T. Chiu, H. Wu, O. J. Schueller and G. M. Whitesides, “Review – fabrication of microfluidic systems in poly (dimethylsiloxane),” *Electrophoresis* vol. 21, no. 1, pp. 27–40, 2000.
- [9] J. N. Lee, C. Park and G. M. Whiteside, “Solvent Compatibility of Poly(dimethylsiloxane)-Based Microfluidic Devices,” *Anal. Chem.*, vol. 75, no. 23, pp. 6544-54, 2003

- [10] M. Seo, C. Paquet, Z. Nie S. Xu and E. Kumacheva, "Microfluidic consecutive flow-focusing droplet generators," *Soft Matter*, vol. 3, no. 8, pp. 986-92, 2007.
- [11] E. Berthier, E. W. K. Young and D. Beebe, "Engineers are from PDMS-land, Biologists are from Polystyrenia," *Lab Chip*, vol. 12, no. 7, pp. 1224-37, 2012.
- [12] B. D Plouffe and S. K. Murthy, "Perspective on microfluidic cell separation: a solved problem?," *Anal. Chem.*, vol. 86, no. 23, pp. 11481– 8, 2014.
- [13] Y.-B. Bang, K.-M. Lee, S. Oh, "5-axis micro milling machine for machining micro parts," *Int. J. Adv. Manuf. Technol.*, vol. 25, no. 9-10, pp. 888-94, 2005.
- [14] C. L. F. Assis, R. T. Coelho, A. R. Rodrigues, "Burr formation during micro end-milling of ultrafine-grained materials," in *EUSPEN 15th Int. Conf. & Exhibition*, Belgium, Leuven, 2015.
- [15] M. E. Wilson, N. Kota, Y. Kim, Y. Wang, D. B. Stolz, P. R. LeDuc and O. B. Ozdoganlar, "Fabrication of circular microfluidic channels by combining mechanical micromilling and soft lithography," *Lab Chip*, vol. 11, no. 8, pp. 1550–5, 2011.
- [16] P. I. Okagbare, J. M. Emory, P. Datta, J. Goettert and S. A. Soper, "Fabrication of a cyclic olefin copolymer planar waveguide embedded in a multi-channel poly(methyl methacrylate) fluidic chip for evanescence excitation," *Lab Chip*, vol. 10, no.1, pp. 66–73. 2010.
- [17] G. S. Fiorini and D. T. Chiu, "Disposable microfluidic devices: fabrication, function, and application," *Biotechniques*, vol. 38, no. 3, pp. 429-46, 2005.
- [18] E. Sollier, C. Murray, P. Maoddi and D. Di Carlo, "Rapid prototyping polymers for microfluidic devices and high pressure injections," *Lab Chip*, vol. 11, no. 22, pp. 3752-65, 2011.
- [19] H. Becker, "Mind the gap!," *Lab Chip*, vol. 10, no. 3, pp. 271-3, 2010.
- [20] A. D. Mazzeo, M. Dirckx and D. E. Hardt, "Process selection for microfluidic device manufacturing," in *Annual Technical Conference: Plastics Encounter*, Ohio, USA, 2007, pp. 1997-2001.

- [21] S. Liao, C. Gerhardy, J. Sackmann, W. K. Schomburg, "Tools for ultrasonic hot embossing," *Microsyst. Technol.*, vol. 21, no. 7, pp. 1533-41, 2015.
- [22] K. Burlage, C. Gerhardy and W. K. Schomburg. *Ultrasonic Hot Embossing and Welding of Micro Structures*. In G. Ananthasuresh, B. Corves, V. Petuya (Eds.), *Micromechanics and Microactuators, Mechanisms and Machine Science*, vol. 2, Springer, Dordrecht, 2011, pp. 113-23.
- [23] D. J. Guckenberger, T. E. de Groot, A. M. D. Wan, D. J. Beebe and E. W. K. Young, "Micromilling: A method for ultra-rapid prototyping of plastic microfluidic devices," *Lab Chip*, vol. 15, no. 11, pp. 2364–78, 2015.
- [24] C.-W. Tsao, "Polymer Microfluidics: Simple, Low-Cost Fabrication Process Bridging Academic Lab Research to Commercialized Production," *Micromachines*, vol. 7, no. 12, pp. 225, 2016.
- [25] L. Cui, C. Gerhardy, W. K. Schomburg, Y. Tian and D. Zhang, "Fabrication of polymer electronic boards by ultrasonic embossing and welding," *Microsyst. Technol.*, vol. 21, no. 2, pp. 365-9, 2013.
- [26] J.-C. Hung, Y.-P. Tsai and C. Hung, "Development of a new apparatus for ultrasonic vibration-assisted glass hot embossing process," *Precis. Eng.*, vol. 37, no.1, pp. 222–7, 2013.
- [27] P. Khuntontong, T. Blaser and W. K. Schomburg, "Fabrication of molded interconnection devices by ultrasonic hot embossing on thin polymer films," *IEEE Trans. Electr. Pack. Manufact.*, vol. 32, no. 3, pp. 152-6, 2009.
- [28] P. Khuntontong, T. Blaser and W. K. Schomburg, "Ultrasonic micro hot embossing of polymer exemplified by a micro thermal flow sensor," in *Proc. of Smart System Integration*, Barcelona, Spain, 2008, pp. 327-34.
- [29] J. Li, C. Gerhardy and W. K. Schomburg, "Polymer circuit boards fabricated by ultrasonic hot embossing," *J. Micromech. Microeng.*, vol. 23, no. 7, pp. 075028, 2013.

- [30] H. Mekar, H. Goto and M. Takahashi, "Development of ultrasonic micro hot embossing technology," *Microelectronic Eng.*, vol. 84, no. 5-8, pp. 1282–7, 2007.
- [31] P. Gielen, R. Sillen and E. Puik, "Low Cost Environmentally Friendly Ultrasonic Embossed Electronic Circuit Board," in *Electronic System-Integration Technology Conf. (ESTC)*, Amsterdam, Netherlands, 2012.
- [32] J. Sackmann, K. Burlage, C. Gerhardy, B. Memering, S. Liao and W. K. Schomburg, "Review on ultrasonic fabrication of polymer micro devices," *Ultrasonics*, vol. 56, pp. 189-200, 2015.
- [33] Y. Luo, X. Yan, N. Qi, X. Wang and L. Wang, "Study of Double-Side Ultrasonic Embossing for Fabrication of Microstructures on Thermoplastic Polymer Substrates," *PloS One*, vol. 8, no. 4, pp. e61647, 2013.
- [34] J. Kosloh, J. Sackmann, R. Šakalys, S. Liao, C. Gerhardy and W. K. Schomburg, "Heat generation and distribution in the ultrasonic hot embossing process," *Microsyst. Technol.*, vol. 23, no. 5, pp. 1411-21, 2017.
- [35] H. Mekar, "Effect of Applying Ultrasonic Vibration in Hot Embossing and Nanoimprint", Lithography Michael Wang, IntechOpen, 2010. Last access date: 5 May 2018. Available from: <https://www.intechopen.com/books/lithography/effect-of-applying-ultrasonic-vibration-in-hot-embossing-and-nanoimprint>.
- [36] P. Khuntontong, Fabrication of Polymer Micro Devices by Ultrasonic Hot Embossing, PhD. Dissertation, Aachen University, Aachen, Germany, 2008.
- [37] C. H. Lee, P. G. Jung, S. M. Lee, S. H. Park, B. S. Shin, J.-H. Kim, K.-Y. Hwang, K. M. Kim and J. S. Ko, "Replication of polyethylene nano-micro hierarchical structures using ultrasonic forming," *J. Micromech. Microeng.*, vol. 20, no. 3, pp. 035018, 2010.
- [38] H. W. Yu, C. H. Lee, P. G. Jung, B. S. Shin, J.-H. Kim and K.-Y Hwang and J. S. Ko, "Polymer microreplication using ultrasonic vibration energy," *J. Micro/Nanolith. MEMS MOEMS*, vol. 8, no. 2, pp. 021113, 2009.

- [39] J. L. Tan, W. J. Lin and Y. C. Lam, "Finite Element Simulation of Ultrasonic Embossing on Polymers," in *13th Int. Conf. on Control, Automation, Robotics & Vision*, Singapore, Singapore, 2014, pp. 1229-33.
- [40] W. Jung, H.-J. Lee and K. Park, "Investigation of Localized Heating Characteristics in Selective Ultrasonic Imprinting," *Int. J. Precis. Eng. Man.*, vol. 16, no. 9, pp. 1999-2004, 2015.
- [41] P. Khuntontong, T. Blaser, D. Maas and W. K. Schomburg, "Fabrication of a polymer micro mixer by ultrasonic hot embossing," in *19th MicroMechanics Europe Workshop*, Barcelona, Spain, 2008, pp. 259-62.
- [42] N. Qi, Y. Luo, X.-D. Wang, L.-D. Wang and Z.-B. Zhang, "Local thermal-assisted ultrasonic embossing for the fabrication of polymer microstructures," *Microsyst. Technol.*, vol. 21, no. 5, pp. 1101-10, 2015.
- [43] J. Xu, J. Li, E. Chen and C. Liu, "Ultrasonic Mechanism of Micro Pattern Replication on Glassy Polymer Films," in *24th Int. Congress on Sound and Vibration*, London, UK, 2017.
- [44] A. Palevičius, G. Janušas, E. Čekas and R. Šakalys, "Analysis of the Influence of High-Frequency Excitation into Quality of the Replicated Microstructure," *Exp. Techniques*, vol. 40, no. 4, pp. 1285-96, 2016.
- [45] R. Šakalys, G. Janušas, A. Palevičius, E. Čekas, V. Jūrėnas, and A. Sodah, "Microstructures replication using high frequency excitation," *Microsyst. Technol.*, vol. 22, no. 7, no., pp. 1831-43, 2016.
- [46] S.-J. Liu, Y.-C. Huang, S.-Y. Yang and K.-H. Hsieh, "Rapid fabrication of surface-relief plastic diffusers by ultrasonic embossing," *Opt. Laser Technol.*, vol. 42, no. 5, pp. 794-8, 2010.
- [47] J. Zhu, Y. Tian, C. Yang, L. Cui, F. Wang, D. Zhang and X. Liu, "Low-cost and fast fabrication of the ultrasonic embossing on polyethylene terephthalate (PET) films using laser processed molds," *Microsyst. Technol.*, vol. 23, no. 12, pp. 5653-68, 2017.

- [48] H. Bae and K. Park, "Design and analysis of ultrasonic horn for polymer sheet forming," *Int. J. Precis. Eng. Manuf.- Green Technol.*, vol. 3, no. 1, pp. 49-54, 2016.
- [49] A. Tollkötter, T. Baldhoff, J. Sackmann, N. Kockmann, W. K. Schomburg, "Modular microfluidic system fabricated from ultrasonic welded foils," in *Proc. 7th Workshop Chemical and Biological Micro Laboratory Technology*, Ilmenau/Elgersburg, Germany, 2014, pp. 10–11.
- [50] K. Burlage, C. Gerhardy, and W. K. Schomburg, "PVDF micro heat exchanger manufactured by ultrasonic hot embossing and welding," in *Proc. of MME 2010: 21st MicroMechanics Europe Workshop*, Enschede, The Netherlands, 2010.
- [51] T. Nieradzic, "Herstellung und Charakterisierung einer mit Ultraschall heißgeprägten ventillosen Mikropumpe," Studienarbeit, Aachen University, Aachen, Germany, 2010.
- [52] L. J. Kricka, P. Fortina, N. J. Panaro, P. Wilding, G. Alonso-Amigo and H. Becker, "Fabrication of plastic microchips by hot embossing," *Lab Chip*, vol. 2, no. 1, pp. 1–4, 2002.
- [53] M. Worgull, *Hot Embossing: Theory and Technology of Microreplication*; William Andrew: Oxford, 2009, p. 368
- [54] G. Cheng, M. Sahli, J.-C. Gelin and T. Barriere, "Physical modeling, numerical simulation and experimental investigation of microfluidic devices with amorphous thermoplastic polymers using a hot embossing process," *J. Mater. Process. Techn.*, vol. 229, pp. 36–53, 2016.
- [55] A. Mathur, S. S. Roy, M. Tweedie, S. Mukhopadhyay, S. K. Mitra and J. A. McLaughlin, "Characterization of PMMA microfluidic channels and devices fabricated by hot embossing and sealed by direct bonding," *Curr. Appl. Phys.*, vol. 9, no. 6, pp. 1199–1202, 2009.
- [56] S.-C. Nian, T.-H. Tsai and M.-S. Huang, "Novel inductive hot embossing for increasing micromolding efficiency," *Int. Commun. Heat Mass*, vol. 70, pp. 38–46, 2016.

- [57] L. Ressler, C. Martin and J. P. Peyrade, "Atomic force microscopy study of micrometric pattern replica by hot embossing lithography," *Microelectron. Eng.*, vol. 71, no. 3–4, pp. 272–6, 2004.
- [58] C. C. Kuo and Y.-J Wang, "Development of a micro-hot- embossing mold with high replication fidelity using surface modification," *Mater. Manuf. Process.*, vol. 29, no. 9, pp. 1101–10, 2014
- [59] C.-C. Kuo and H.-J. Hsu, "Development and application of hybrid mold with microfeatures in micro-hot embossing," *Mater. Manuf. Process.*, vol. 28, no. 11, pp. 1203–8, 2013.
- [60] J. M. Li, C. Liu and J. Peng, "Effect of hot embossing process parameters on polymer flow and microchannel accuracy produced without vacuum," *J. Mater. Process. Techn.*, vol. 207, no. 1–3, pp. 163–71, 2008.
- [61] D. Konstantinou, A. Shirazi, A. Sadri and E. W. K. Young, "Combined hot embossing and milling for medium volume production of thermoplastic microfluidic devices," *Sensor Actuat. B-Chem.*, vol. 234, pp. 209–21, 2016.
- [62] Y. He, W. Wu, T. Zhang and J. Fu, "Micro structure fabrication with a simplified hot embossing method," *RSC Advances*, vol. 5, no. 49, pp. 39138–44, 2015.
- [63] R. K. Jena, C.Y. Yue, Y. C. Lam, P. S. Tang and A. Gupta, "Comparison of different molds (epoxy, polymer and silicon) for microfabrication by hot embossing technique," *Sensor. Actuat. B-Chem.*, vol. 163, no. 1, pp. 233–41, 2012.
- [64] M. C. Lin, J. P. Yeh, S. C. Chen, R.-D. Chien, C.-L. Hsu, "Study on the replication accuracy of polymer hot embossed microchannels," *Int. Commun. Heat Mass*, vol. 42, pp. 55–61, 2013.
- [65] C. Liu, J. M. Li, J. S. Liu and L. D. Wang, "Deformation behavior of solid polymer during hot embossing process," *Microelectron. Eng.*, vol. 87, no. 2, pp. 200–7, 2010.

- [66] F. Coğun, E. Yıldırım and M. A. S. Arıkan, "Investigation on replication of microfluidic channels by hot embossing," *Mater. Manuf. Processes*, vol. 32, no. 16, pp. 1838-44, 2017.
- [67] M. D. Abramoff, P. J. Magalhaes and S. J. Ram, "Image Processing with ImageJ," *Biophotonics International*, vol. 11, no. 7, pp. 36-42, 2004.
- [68] C. Liu, J. M. Li, J. S. Liu and L. D. Wang, "Deformation behavior of solid polymer during hot embossing process," *Microelectron. Eng.*, vol. 87, no. 2, pp. 200-207, 2010.
- [69] S. Moore, J. Gomez, D. Lek, B. H. You, N. Kim and I.-H. Song, "Experimental study of polymer microlens fabrication using partial-filling hot embossing technique," *Microelectron. Eng.*, vol. 162, pp. 57-62, 2016.
- [70] X. Zhang, G. Fang, T. Jiang, N. Zhao, J. Li, B. Dun and Q. Li, "Effects of cavity size and density on polymer micro hot embossing," *Int. J. Precis. Eng. Man.*, vol. 16, no. 11, pp. 2339-2346, 2015.
- [71] P. Goos and D. Meintrup, *Statistics with JMP: Hypothesis Tests, ANOVA and Regression*, John Wiley & Sons: West Sussex, 2016, p. 648.
- [72] H. Becker, "Mind the gap!," *Lab Chip*, vol. 10, no. 3, pp. 271-273, 2010.
- [73] I. R. G. Ogilvie, V. J. Sieben, C. F. A. Floquet, R. Zmijan, M. C. Mowlem and H. Morgan, "Reduction of surface roughness for optical quality microfluidic devices in PMMA and COC," *J. Micromech. Microeng.*, vol. 20, no. 6, p. 065016, 2010.
- [74] J. Jiang, J. Zhan, W. Yue, M. Yang, C. Yi and C.-W. Li, "A single low-cost microfabrication approach for polymethylmethacrylate, polystyrene, polycarbonate and polysulfone based microdevices," *RSC Adv.*, vol. 5, no. 45, pp. 36036-36043, 2015.
- [75] J. N. Lee, C. Park and G. M. Whiteside, "Solvent Compatibility of Poly(dimethylsiloxane)-Based Microfluidic Devices," *Anal. Chem.* vol. 75, no. 23, pp. 6544-54, 2003.

- [76] M. Seo, C. Paquet, Z. Nie, S. Xu and E. Kumacheva, "Microfluidic consecutive flow-focusing droplet generators," *Soft Matter*, vol. 3, no. 8, pp. 986-92, 2007.
- [77] L. J. Kricka, P. Fortina, N. J. Panaro, P. Wilding, G. Alonso-Amigo and H. Becker "Fabrication of plastic microchips by hot embossing," *Lab Chip*, vol. 2, no. 1, pp. 1-4, 2002.
- [78] E. Berthier, E. W. K. Young and D. Beebe, "Engineers are from PDMS-land, Biologists are from Polystyrenia," *Lab Chip*, vol. 12, no. 7, pp. 1224-37, 2012.
- [79] M. Demiral, "Smoothed particle hydrodynamics modeling of vibro-assisted turning of Ti alloy: influence of vibration parameters," *J. Vibroeng.*, vol. 16, no. 6, pp. 2685-94, 2014.
- [80] Y. Mizuno and K. Nakamura, "Brillouin Scattering in Polymer Optical Fibers: Fundamental Properties and Potential Use in Sensors," *Polymers*, vol. 3, no. 2, pp. 886-98, 2011.
- [81] P. Moy, C. A. Gunnarsson, T. Weerasooriya and W. Chen, "Stress-Strain Response of PMMA as a Function of Strain-Rate and Temperature," *Dynamic Behavior of Materials*, vol. 1, pp. 125-33, 2011.
- [82] W. M. Cheng, G. A. Miller, J. A. Manson, R. W. Hertzberg and L. H. Sperling, "Mechanical behaviour of poly(methylmethacrylate) - Part 1 Tensile strength and fracture toughness," *J. Mater. Sci.*, vol. 25, no. 4, pp. 1917-23, 1990.
- [83] A. S. Nanu, N. I. Marinescu and D. Ghiculescu, "Study on ultrasonic stepped horn geometry design and FEM simulation," *Nonconventional Technologies Review*, vol. 15, no. 4, pp. 25-30, 2011.
- [84] J. Grabalosa, I. Ferrera, O. Martínez-Romero, A. Elías-Zúñiga, X. Plantá and F. Rivillas, "Assessing a stepped sonotrode in ultrasonic molding technology," *J. Mater. Process. Techn.*, vol. 229, pp. 687-96, 2016.
- [85] M. Nad, "Ultrasonic horn design for ultrasonic machining technologies," *Applied and Computational Mechanics*, vol. 4, no. 1, pp. 79-88, 2010.

- [86] K.-M. Shu, W.-H. Hsieh and H.-S. Yen, "On the design and analysis of acoustic horns for ultrasonic welding," *T. Can. Soc. for Mech. Eng.*, vol. 37, no. 3, pp. 905-16, 2013.
- [87] FLIR Systems, *FLIR Ex Series: User's Manual*, 2013.
- [88] I. R. G. Ogilvie, V. J. Sieben, C. F. A. Floquet, R. Zmijan, M. C. Mowlem and H. Morgan, "Reduction of surface roughness for optical quality microfluidic devices in PMMA and COC," *J. Micromech. Microeng.*, vol. 20, no. 6, pp. 065016, 2010.
- [89] J. Wu and M. Gu, "Microfluidic sensing: state of the art fabrication and detection techniques," *J. Biomedical Optics*, vol. 16, no. 8, pp. 080901, 2011.
- [90] E. K. Sackmann, A. L. Fulton and D. J. Beebe, "The present and future role of microfluidics in biomedical research," *Nature*, vol. 507, no. 7491, pp. 181-9, 2014.
- [91] M. I. Mohammed, S. Haswell and I. Gibson, "Lab-on-a-chip or Chip-in-a-lab: Challenges of Commercialization Lost in Translation," *Procedia Technology*, vol. 20, pp. 54-9, 2015.
- [92] W. Zhang, S. Lin, C. Wang, J. Hu, C. Li, Z. Zhuang, Y. Zhou, R. A. Mathies and C. J. Yang, "PMMA/PDMS Valves and Pumps for Disposable Microfluidics," *Lab Chip*, vol. 9, no. 21, pp. 3088-94, 2009.
- [93] Y. Chen, L. Zhang and G. Chen, "Fabrication, Modification, and Application of Poly(methyl Methacrylate) Microfluidic Chips," *Electrophoresis*, vol. 29, no. 9, pp. 1801-14, 2008.
- [94] K. Jensen and A. P. Lee, "The science & applications of droplets in microfluidic devices-Foreword," *Lab Chip*, vol. 4, no. 4, pp. 31N-32N, 2004.
- [95] D. Belder, "Microfluidics with droplets," *Angew. Chem. Int. Ed.* vol. 44, no. 23, pp. 3521-2, 2005.
- [96] I. Kobayashi, K. Uemura and M. Nakajima, "Formulation of monodisperse emulsions using submicron-channel arrays," *Colloid. Surf. A Physicochem. Eng. Asp.*, vol. 296, no. 1-3, pp. 285-9, 2007.

- [97] Y. C. Huang, C. C. Chan, W. T. Lin, H. Y. Chiu, R. Y. Tsai, T. H. Tsai, J. Y. Chan, S. J. Lin, “Scalable production of controllable dermal papilla spheroids on PVA surfaces and the effects of spheroid size on hair follicle regeneration,” *Biomaterials*, vol. 34, no. 2, pp. 442–51, 2013.
- [98] J. M. Kelm, V. Djonov, S. P. Hoerstrup, C. I. Guenter, L. M. Ittner, F. Greve, A. Hierlemann, C. D. Sanchez-Bustamante, J. C. Perriard, E. Ehler, M. Fussenegger, “Tissue-transplant fusion and vascularization of myocardial microtissues and macro tissues implanted into chicken embryos and rats,” *Tissue Eng.*, vol. 12, no. 9, pp. 2541–53, 2006.
- [99] J. M. Kelm, V. Djonov, L. M. Ittner, D. Fluri, W. Born, S. P. Hoerstrup, M. Fussenegger, “Design of custom-shaped vascularized tissues using microtissue spheroids as minimal building units,” *Tissue Eng.*, vol. 12, no. 8, pp. 2151–60, 2006.
- [100] B. S. Schon, K. Schrobback, M. van der Ven, S. Stroebel, G. J. Hooper, T. B. Woodfield, “Validation of a high-throughput microtissue fabrication process for 3D assembly of tissue engineered cartilage constructs,” *Cell Tissue Res.*, vol. 347, no. 3, pp. 629–642, 2012.
- [101] S. Mashaghi, A. Abbaspourrad, D. A. Weitz, A. M. van Oijen, “Droplet microfluidics: A tool for biology, chemistry and nanotechnology,” *Trends in Analyt. Chem.*, vol. 82, pp. 118–25, 2016.
- [102] S.-Y. Teh, R. Lin, L.-H. Hung and A. P. Lee, “Droplet microfluidics,” *Lab Chip*, vol. 8, no. 2, pp. 198–220, 2008.
- [103] L. Shang, Y. Cheng, and Y. Zhao, “Emerging Droplet Microfluidics,” *Chem. Rev.*, vol. 117, no. 12, pp. 7964–8040, 2017.
- [104] C. N. Baroud, F. Gallaire and R. Danga, “Dynamics of microfluidic droplets,” *Lab Chip*, vol. 10, no. 16, pp. 2032–45, 2010.
- [105] H. Gu, M. H. G. Duits and F. Mugele, “Droplets Formation and Merging in Two-Phase Flow Microfluidics,” *Int. J. Mol. Sci.*, vol. 12, no. 4, pp. 2572–97, 2011.

- [106] A. S. Basu, “Droplet morphometry and velocimetry (DMV): a video processing software for time-resolved, label-free tracking of droplet parameters,” *Lab Chip*, vol. 13, no.10, pp. 1892-901, 2013.
- [107] A. S. Hoffman, “Hydrogels for biomedical applications,” *Adv. Drug Deliv. Rev.*, vol. 64, pp. 18-23, 2012.
- [108] Y. Morimoto and S.Takeuchi, “Three-dimensional cell culture based on microfluidic techniques to mimic living tissues,” *Biomater. Sci.*, vol. 1, pp. 257–64, 2013.
- [109] C. Y. Li, D. K. Wood, C. M. Hsu, and S. N. Bhatia, “DNA-templated assembly of droplet-derived PEG microtissues,” *Lab Chip*, vol. 11, no. 17, pp. 2967–75, 2011.

CURRICULUM VITAE

PERSONAL INFORMATION

Surname, Name: Çoğun, Ferah
Nationality: Turkish (TC)
Date and Place of Birth: 27 May 1990, Riyad
Marital Status: Single
Phone: +90 312 233 13 30
email: ferahco@cankaya.edu.tr

EDUCATION

Degree	Institution	Year of Graduation
MS	METU, Mechanical Engineering	2013
BS	Başkent Univ., Mechanical Engineering	2011
High School	Gazi Univ. Foundation Private Sci. High School	2007

WORK EXPERIENCE

Year	Place	Enrollment
2014- Present	Çankaya Univ., Dept. of Mech. Eng.	Research Assistant

FOREIGN LANGUAGES

English.

PUBLICATIONS

Journal Articles

- 1) C. Cogun, Z. Esen, A. Genc, **F. Cogun** and N. Akturk, “The Effect of PM Cu-B₄C Electrodes on Workpiece Surface Characteristics and Machining Performance of EDM,” Proc. Inst. Mech. Eng. B J. Eng. Manuf., vol. 230, no. 12, pp. 2190-2203, 2016.
- 2) **F. Cogun** and H. Darendeliler, “Comparison of different yield criteria in various deep drawn cups,” Int. J. Mater. Form., vol. 10, no. 1, pp. 85-98, 2017.

- 3) **F. Çoğun**, E. Yıldırım and M.A.S. Arıkan, “Investigation on Replication of Microfluidic Channels by Hot Embossing,” *Mater. Manuf. Process.*, vol. 32, no. 16, pp. 1838-1844, 2017.
- 4) B. Gjergjizi, **F. Cogun**, E. Yıldırım, M. Eryılmaz, Y. Selbes, N. Sağlam and U. Tamer, “SERS Based Ultrafast and Sensitive Detection of Luteinizing Hormone In Human Serum Using A Passive Channel Microchip,” *Sens. Actuators B Chem.*, 2018, doi: 10.1016/j.snb.2018.05.001 (published electronically).
- 5) Kasap, E. N, Dogan, U., **Çoğun**, F., Yıldırım E., Boyacı I. H., Çetin D., Suludere, Z., Tamer, U., “Rapid And Selective Determination of Bacteria by Using Passive Microfluidic Chip,” 2018 (submitted).
- 6) **F. Cogun**, M. A. S. Arıkan, and E. Yildirim, “Experimental and Numerical Investigation of Ultrasonic Embossing for Fabrication of Thermoplastic Microfluidic Chips,” 2018 (submitted).

Conference Papers

- 1) **F. Çoğun**, F. Alkan and F. Elaldı, “Design, Manufacture and Implementation of Sheet Metal Hydroforming System,” 6th Int. Conf. and Exhibition on Design and Production of Machines and Dies/Molds, June 23-26, Atılım University, Ankara, 2011.
- 2) F. Alkan, **F. Çoğun** and F. Elaldı, “Sıvı Basıncı ile Sac Şekillendirme (Hydroforming) Sisteminin Tasarımı, İmalatı ve Denenmesi,” 6th National Hydraulic Pneumatic Congress and Exhibition, Oct. 12-15, İzmir, 2011 (text in Turkish).
- 3) A. Ziyara, **F. Çoğun**, C. Varol, O. Totuk and E. Yıldırım, “Optimization of Hot Embossing Process for Fabrication of Microfluidic Devices,” 8th Engineering and Technology Symposium, May 14-15, Cankaya University, Ankara, 2015 (text in English).
- 4) **F. Cogun**, V. Esat and R. O. Yildirim, “Comparison of Analytical and Numerical Approaches for the Effect of Die and Tube Parameters on Tube Expansion

Process,” 8th Int. Conf. and Exhibition on Design and Production of Machines and Dies/Molds, June 18-21, pp.67-71, Kuşadası, Aydın, 2015.

- 5) E. N. Kasap, **F. Çoğun**, E. Yıldırım, İ. H. Boyacı, D. Çetin, Z. Suludere, U. Tamer, N. Ertas, “Microchip Based Determination of Bacteria by In-Chip Sandwich Immunoassay,” Int. Multidisciplinary Symposium on Drug Research and Development, October 15-17, Eskişehir 2015 (poster presentation).
- 6) **F. Çoğun**, E. Yıldırım and M. Parsian, “Effect of preheating on channel geometry and surface texture in fabrication of plastic microfluidic chips by ultrasonic hot embossing,” Microfluidics 2016, July 24-26, Heidelberg, Germany, 2016 (poster presentation).
- 7) E. E. Ahi, A. Gumustas, H. Çiftçi, M. G. Caglayan, Y. S. Selbes, **F. Çoğun**, E. Yıldırım, U. Tamer, “Chip-Based Immunomagnetic Separation of Human Chorionic Gonadotropin,” 10th Aegean Analytical Chemistry Days, 29 Sept. - 2 Oct., Çanakkale, 2016 (poster presentation) (poster award).
- 8) U. Dogan, E. Kasap, **F. Çoğun**, E. Yıldırım, D. Cetin, Z. Suludere, İ. H. Boyacı, N. Ertas, U. Tamer, “Simultaneous Detection of Two Different Bacteria Using QDs and MNPs,” 10th Aegean Analytical Chemistry Days, 29 Sept. - 2 Oct., Çanakkale, 2016 (poster presentation).
- 9) U. Dogan, E. N. Kasap, **F. Cogun**, E. Yildirim, D. Cetin, Z. Suludere, I. H. Boyacı, N. Ertas, U. Tamer, “Simultaneous Detection of E. Coli and Salmonella Based on Fluorescence Technique in a Passive Type Microfluidic Chip,” 2nd Int. Gazi Pharma Symposium Series (GPSS-2017), 11-13 October 2017, Gazi University, Ankara.

HOBBIES

Sports, Movies, Music, Resin Crafts, Glass Engraving.